



University of Dundee

Accelerated cell divisions drive the outgrowth of the regenerating spinal cord in axolotls

Rost, Fabian; Rodrigo Albers, Aida; Mazurov, Vladimir; Brusch, Lutz; Deutsch, Andreas; Tanaka, Elly M.; Chara, Osvaldo

Published in:
eLife

DOI:
[10.7554/eLife.20357](https://doi.org/10.7554/eLife.20357)

Publication date:
2016

Document Version
Peer reviewed version

[Link to publication in Discovery Research Portal](#)

Citation for published version (APA):

Rost, F., Rodrigo Albers, A., Mazurov, V., Brusch, L., Deutsch, A., Tanaka, E. M., & Chara, O. (2016). Accelerated cell divisions drive the outgrowth of the regenerating spinal cord in axolotls. eLife. DOI: 10.7554/eLife.20357

General rights

Copyright and moral rights for the publications made accessible in Discovery Research Portal are retained by the authors and/or other copyright owners and it is a condition of accessing publications that users recognise and abide by the legal requirements associated with these rights.

- Users may download and print one copy of any publication from Discovery Research Portal for the purpose of private study or research.
- You may not further distribute the material or use it for any profit-making activity or commercial gain.
- You may freely distribute the URL identifying the publication in the public portal.

Take down policy

If you believe that this document breaches copyright please contact us providing details, and we will remove access to the work immediately and investigate your claim.

Accelerated cell divisions drive the outgrowth of the regenerating spinal cord in axolotls

Fabian Rost^{1†}, Aida Rodrigo Albors^{2,3,4†}, Vladimir Mazurov^{3,4}, Lutz Brusch^{1,5}, Andreas Deutsch^{1,5}, Elly M. Tanaka^{3,4‡*} and Osvaldo Chara^{1,6‡*}

¹ Center for Information Services and High Performance Computing, Technische Universität Dresden, Dresden, Germany

² Present address: Division of Cell & Developmental Biology, School of Life Sciences, University of Dundee, Dundee, United Kingdom

³ Deutsche Forschungsgemeinschaft – Center for Regenerative Therapies Dresden, Dresden, Germany

⁴ Max Planck Institute of Molecular Cell Biology and Genetics, Dresden, Germany

⁵ Center for Advancing Electronics Dresden (cfaed), 01062 Dresden, Germany

⁶ Systems Biology Group (SysBio), Institute of Physics of Liquids and Biological Systems, National Scientific and Technical Research Council (CONICET) and University of La Plata, La Plata, Argentina

† Co-first authorship

‡ Co-last authorship

* Corresponding authors

Corresponding authors:

Osvaldo Chara

Center for Information Services and High Performance Computing, Technische Universität Dresden, Nöthnitzer Straße 46, 01187 Dresden, Germany

Tel. +49 351 463-38780

E-mail: osvaldo.chara@tu-dresden.de

Systems Biology Group (SysBio), Institute of Physics of Liquids and Biological Systems (IFlySIB), National Scientific and Technical Research Council (CONICET) and University of La Plata

Calle 59 N 789, 1900 La Plata, Argentina

Tel. +54 221 4233283 Ext: 26

E-mail: ochara@iflysib.unlp.edu.ar

Elly Tanaka

Deutsche Forschungsgemeinschaft – Center for Regenerative Therapies Dresden (CRTD)

Fetscherstraße 105, 01307 Dresden, Germany

Tel. +49 351 458-82000

E-mail: elly.tanaka@crt-dresden.de

40 **Abstract**

41 Axolotls are unique in their ability to regenerate the spinal cord. However, the mechanisms that
42 underlie this phenomenon remain poorly understood. Previously, we showed that regenerating stem
43 cells in the axolotl spinal cord revert to a molecular state resembling embryonic neuroepithelial cells
44 and functionally acquire rapid proliferative divisions (Rodrigo Albors et al., 2015). Here, we refine the
45 analysis of cell proliferation in space and time and identify a high-proliferation zone in the regenerating
46 spinal cord that shifts posteriorly over time. By tracking sparsely-labeled cells, we also quantify cell
47 influx into the regenerate. Taking a mathematical modeling approach, we integrate these quantitative
48 datasets of cell proliferation, neural stem cell activation and cell influx, to predict regenerative tissue
49 outgrowth. Our model shows that while cell influx and neural stem cell activation play a minor role, the
50 acceleration of the cell cycle is the major driver of regenerative spinal cord outgrowth in axolotls.

51 **Introduction**

52 Neural stem cells exist in the spinal cord of all vertebrates, but only in salamanders these cells
53 are mobilized efficiently to resolve spinal cord injuries (Becker & Becker, 2015; Tanaka and Ferretti,
54 2009). In axolotls, this is best exemplified following tail amputation, when cells adjacent to the cut end
55 regrow a fully functional spinal cord (Holtzer, 1956; Mchedlishvili *et al.*, 2007). Despite the
56 regenerative potential of axolotl neural stem cells, little was known about the molecular changes
57 occurring upon them and the changes in cell behavior that lead to the rapid expansion of the stem cell
58 pool during regeneration.

59 In our previous study, we looked at spinal cord regeneration at the molecular and cellular
60 levels. There, we found that resident SOX2⁺ neural stem cells re-activate an embryonic-like gene
61 expression program following tail amputation (Rodrigo Albors *et al.*, 2015). Part of this program
62 involves the re-establishment of planar cell polarity (PCP) signaling, the downregulation of pro-neural
63 genes, and upregulation of proliferation-promoting genes. In line with these gene expression changes,
64 we also found that regenerating neural stem cells speed up their cell cycle, and switch from neuron-
65 generating to proliferative cell divisions. PCP turned out to be key for the efficient and orderly
66 expansion of the regenerating spinal cord, at least in part by instructing cells to divide along the
67 growing axis. However, besides oriented cell division, whether other cellular mechanisms such as
68 convergence and extension, which leads to the narrowing and lengthening of tissues, are involved in
69 the rapid expansion of the regenerating spinal cord remained unknown.

70 In this follow-up study we investigate the contribution of different cellular mechanisms to the
71 elongation of the regenerating spinal cord in the axolotl. To address this question, we apply a
72 quantitative modeling approach to causally link previous (Rodrigo Albors *et al.*, 2015) and new
73 datasets to the time-course of spinal cord outgrowth. In particular, we calculate neural stem cell
74 density from previous measurements (Rodrigo Albors *et al.*, 2015) to show that convergence and
75 extension is negligible. We make use of cell proliferation-related measurements along the anterior-
76 posterior axis (AP) of the spinal cord (Rodrigo Albors *et al.*, 2015) to identify a high-proliferation zone,
77 which initially extends 800 μm anterior to the amputation plane, and calculate changes in cell cycle
78 kinetics within this zone. By tracing sparsely-labelled cells, we also determine cell influx into the
79 regenerating spinal cord. Finally, we set up a mathematical model of spinal cord outgrowth that
80 incorporates cell proliferation, neural stem cell activation, and cell influx. Using this model, we test the
81 contribution of each of these cellular mechanisms to the regenerative spinal cord outgrowth.
82 Comparing the model predictions with experimental data of tissue outgrowth we show that while cell
83 influx and activation of quiescent neural stem cells play a minor role, the acceleration of the cell cycle
84 in the high-proliferation zone is the major driver of the observed regenerative spinal cord outgrowth.

85 **Results**

86 **The regenerating spinal cord grows with increasing velocity**

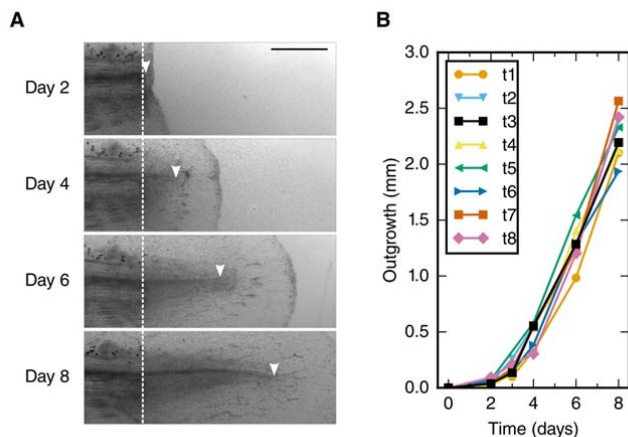
87 To refine the outgrowth time-course of the regenerating spinal cord, we measured the spinal
88 cord outgrowth in individual axolotls, 2-3 cm snout to tail, during the first 8 days of regeneration (Figure
89 1A, Figure 1 – figure supplement 1 and Supplementary file 1). Initially, the regenerating spinal cord
90 extended slowly to a mean outgrowth of 0.45 ± 0.04 mm at day 4 (Figure 1B). Thereafter, the spinal
91 cord grew faster, reaching an outgrowth of 2.26 ± 0.07 mm by day 8.

92 **The density of neural stem cells stays constant along the AP axis of the regenerating** 93 **spinal cord**

94 To explain the outgrowth time-course of the regenerating spinal cord in terms of underlying
95 cellular mechanisms, we first set out to translate tissue outgrowth into cell numbers. To quantitatively
96 investigate neural stem cell arrangement in space and time, we revisited our previously published
97 dataset of the number of SOX2⁺ cells per cross section in uninjured and regenerating spinal cords
98 (Figure 2A and see Materials and methods) (Rodrigo Albors *et al.*, 2015). We found that the number of

99 SOX2⁺ cells per spinal cord cross section is constant along the AP axis in both uninjured and
 100 regenerating samples at any time (Figure 2B,B' and Figure 2 – figure supplement 1 and see Materials
 101 and methods). We also found that the number of SOX2⁺ cells per cross section spatially averaged
 102 along the AP axis is constant during regeneration (Figure 2C and see Materials and methods). On
 103 average, 30.4 ± 0.6 SOX2⁺ cells make up the circumference of the axolotl spinal cord. Since the length
 104 of SOX2⁺ cells along the AP axis does not change during regeneration ($l_c = 13.2 \pm 0.1 \mu\text{m}$) (Rodrigo
 105 Albors *et al.*, 2015), the density of cells along the AP axis is spatially homogeneous and equal to $2.3 \pm$
 106 0.6 cells/ μm (Figure 2A).

107 Taken together, these findings allow us to exclude mechanisms such as cell shape changes
 108 and convergence and extension as driving forces of regenerative spinal cord outgrowth in the axolotl.
 109 Instead, constant neural stem cell density implies an increasing neural stem cell number during
 110 regeneration. This suggests that the expansion of the regenerating neural stem cell pool mostly relies
 111 on proliferation-based mechanisms.



112
 113 **Figure 1. Spinal cord outgrowth time-course during regeneration (A)** Representative images of a
 114 regenerating spinal cord after tail amputation (individual time-lapse images are in Figure 1 – figure supplement 1).
 115 The white dashed line marks the amputation plane. The arrowheads mark the tip of the regenerating spinal cord.
 116 Scale bar, 1mm. **(B)** Spinal cord outgrowth time-course during the first 8 days after amputation (n = 8 axolotls).

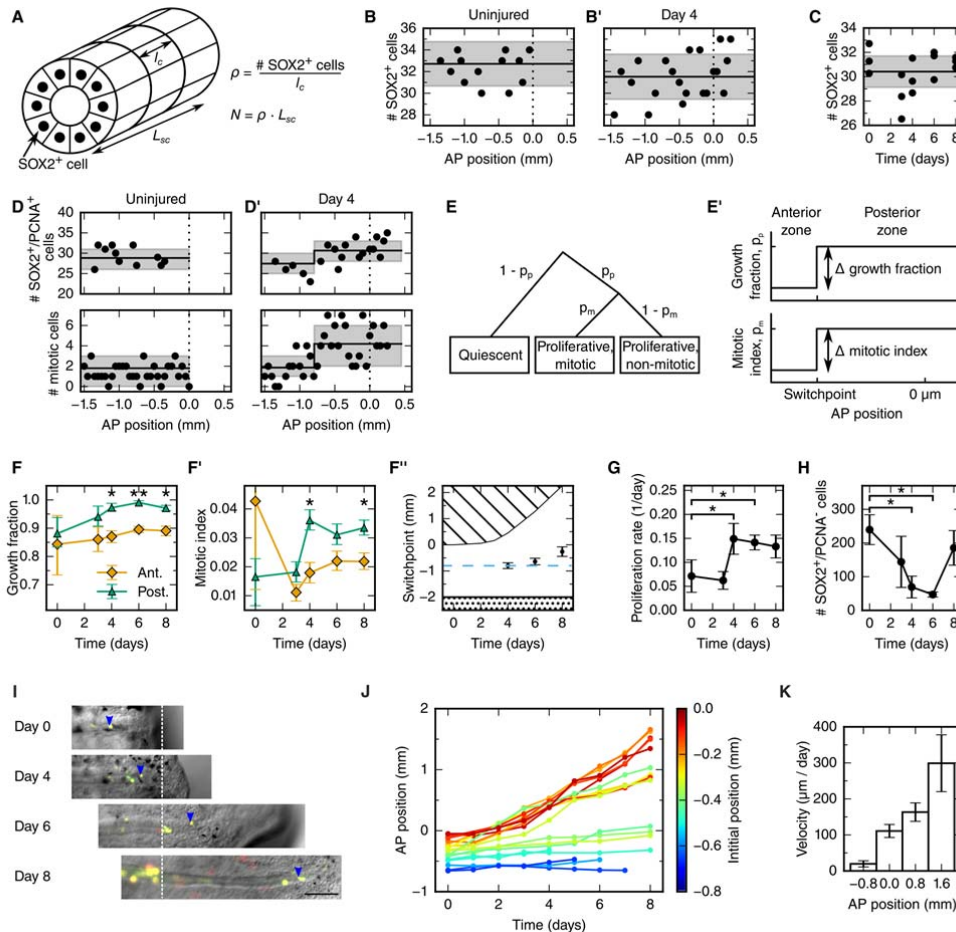
117 **Cell proliferation increases within an 800 μm zone anterior to the amputation plane in 4-day**
 118 **regenerates**

119 To determine spatial and temporal changes in cell proliferation during regeneration, we
 120 calculated different cell proliferation parameters along uninjured and regenerating spinal cords. In our

121 previous study, we quantified the number of proliferative cells, i.e. SOX2⁺ cells that are positive for
122 proliferating cell nuclear antigen (PCNA) and the number of cells in mitosis, i.e. SOX2⁺/PCNA⁺ cells
123 with condensed chromosomes based on Hoechst DNA stain (Rodrigo Albors *et al.*, 2015). Here, we
124 used these datasets to estimate the growth fraction, i.e. the fraction of proliferative cells and the mitotic
125 index, i.e. the ratio of mitotic cells over proliferative cells. Although neither SOX2⁺/PCNA⁺ cells nor
126 mitotic cells showed any evident spatial pattern along the AP axis in uninjured animals (Figure 2D,
127 points), they showed a tendency to increase posteriorly from day 4 (Figure 2D', points). To elucidate
128 whether proliferation was patterned along the AP axis during regeneration, we tested the data with a
129 mathematical model of two spatially homogeneous zones characterized by their growth fraction and
130 mitotic index and separated by a border that we call the *switchpoint* (Figure 2E, E'). We reasoned that
131 in the absence of an AP pattern of cell proliferation the two zones would be indistinguishable; while if
132 cell proliferation would be locally increased, the model would allow us to determine the magnitude and
133 the location of the increased cell proliferation. For a given growth fraction and mitotic index, the model
134 predicts the expected number of proliferative cells and mitotic cells per cross section (Figure 2 – figure
135 supplement 2). Hence, we fitted the model to the cell number datasets of uninjured and regenerating
136 spinal cords at day 3, 4, 6 and 8 after amputation (Figure 2D,D', Figure 2 – figure supplement 3 and
137 Figure 2 – figure supplement 4) to determine the growth fraction, the mitotic index, and the switchpoint
138 for each time point (Figure 2F-F''). Not surprisingly, we found that in the uninjured spinal cord the
139 growth fraction and the mitotic index in the two modeled zones are not significantly different (Figure
140 2D,F,F' and Figure 2 – figure supplement 3). Similarly, at day 3 there are no significant differences
141 between the two zones (Figure 2F,F' and Figure 2 – figure supplement 3). In contrast, the growth
142 fraction and the mitotic index are higher in the posterior zone from day 4 onward (Figure 2D', F, F' and
143 Figure 2 – figure supplement 3). These findings reveal that a high-proliferation zone emerges in the
144 regenerating spinal cord at day 4. At this time point, the switchpoint between the two zones is located
145 $800 \pm 100 \mu\text{m}$ anterior to the amputation plane, but shows the tendency to shift posteriorly as the
146 regenerating spinal cord grows (Figure 2F'').

147 Next, we combined the mitotic index measurements with our previous cell cycle length
148 estimates (Rodrigo Albors *et al.*, 2015) to establish how the proliferation rate changes during
149 regeneration (Figure 2G and see Material and methods). We find that the proliferation rate is
150 0.06 ± 0.02 per day in the uninjured spinal cord which corresponds to a cell cycle length of 10 ± 4 days

151 (Figure 2 – figure supplement 5). The proliferation rate is similar at day 3. However, at day 4 the
 152 proliferation rate increases to about 0.15 per day corresponding to a cell cycle length of about 5 days
 153 and the proliferation rate remains that high until day 8.



154
 155 **Figure 2. Cellular mechanisms underlying spinal cord outgrowth.** (A) Sketch of measurements taken to
 156 estimate the density and total number of neural stem cells (nuclei, black dots) in the axolotl spinal cord. The
 157 density of SOX2⁺ cells, ρ , is the ratio of the number of SOX2⁺ cells per cross section (# stem cells) and the mean
 158 AP cell length, l_c . The density of SOX2⁺ cells is the proportionality constant between the total number of stem cells
 159 in a zone along the spinal cord with zone length, L_{SC} . (B,B') Number of SOX2⁺ cells per cross section along the
 160 AP axis of a selected uninjured (B) and a selected day 4-regenerating spinal cord (B'). Black line and gray region
 161 indicate the mean number of SOX2⁺ cells and the standard deviation, respectively. Plots for all individual axolotls
 162 in Figure 2 – figure supplement 1. (C) Spatial average of the number of SOX2⁺ cells per cross section of individual
 163 axolotls against time (black dots). Black line and gray region indicate the mean number of SOX2⁺ cells and the
 164 standard deviation of all animals, respectively. (D,D') Number of SOX2⁺/PCNA⁺ cells per cross section (upper
 165 panel) and mitotic cells per section (lower panel) along the AP axis in a selected uninjured (D) and a selected day
 166 4-regenerating spinal cord (D'). Black line and the gray region show the expected number and the 68%
 167 confidence belt for the best fit of the model with two spatial proliferation zones, respectively. Plots for all animals
 168 in Figure 2 – figure supplement 3. (E) Possible cell states in the two spatial proliferation zones model used to
 169 analyze the spatial cell proliferation dataset (D,D'). p_p , probability that a cell is proliferative, otherwise quiescent.

170 p_m , probability that a proliferative cell undergoes mitosis at the time of analysis. **(E')** The model assumes two
171 proliferation zones. The location of the border between zones is called *switchpoint*. **(F-F')** Results of model fitting
172 for growth fraction (F) and mitotic index time-course (F') in the anterior (orange diamonds) and posterior (green
173 triangles) zone. Error bars indicate the 68% credibility interval. **(F'')** Black dots mark the switchpoint. Blue dashed
174 line marks 800 μm anterior to the amputation plane. The dashed region marks the space outside of the embryo,
175 the dotted region marks the unaffected part of the embryo. **(G)** Proliferation rate time-course in the high-
176 proliferation zone. **(H)** Total number of $\text{SOX2}^+/\text{PCNA}^-$ cells in the high-proliferation zone (mean \pm linearly
177 propagated $1-\sigma$ error). **(I)** Selected time-lapse images of clone (blue arrowhead) tracking during spinal cord
178 regeneration. Dashed line marks the amputation plane. **(J)** Tracking of 19 clones along the AP axis during
179 regeneration. Clone trajectories are color coded by their initial position. **(K)** Clone velocities at different positions
180 along the AP axis.

181 **Quiescent neural stem cells re-enter the cell cycle during regeneration**

182 Two possible scenarios could lead to the observed increased growth fraction in the high-
183 proliferation zone (Fig. 2F): the activation of quiescent neural stem cells, or the dilution of quiescent
184 cells by the expansion of the proliferating cell population. If quiescent cells were activated, the total
185 number of quiescent cells in the high-proliferation zone would decrease. We estimated the total
186 number of quiescent cells in the high-proliferation zone from the mean number of $\text{SOX2}^+/\text{PCNA}^-$ cells
187 per cross section, the mean AP cell length, and the outgrowth time-course (see Materials and
188 methods). The number of $\text{SOX2}^+/\text{PCNA}^-$ cells drops from 180 ± 30 at day 0 to 23 ± 13 at day 6 (Figure
189 2H) which suggests that quiescent SOX2^+ cells get activated and re-enter the cell cycle upon injury.
190 The number of quiescent SOX2^+ cells appears to increase again at day 8, when cells resume
191 neurogenesis (Rodrigo Albors *et al.*, 2015).

192 **Cells translocate faster the closer they are to the tip of the regenerate**

193 Cell movement could also contribute new cells to the regenerative spinal cord outgrowth. To
194 investigate whether anterior spinal cord cells move into the high-proliferation zone, we followed
195 individual cells during regeneration. For that, we co-electroporated cytoplasmic GFP and nuclear
196 mCherry plasmids at very low concentration to achieve sparse labelling of cells and tracked them daily
197 during the first 8 days of regeneration (Figure 2I). We found that labelled cells preserve their original
198 spatial order: cells located close to the amputation plane end up at the posterior end of the
199 regenerated spinal cord (Figure 2J). Most-anterior cells, however, almost do not change their position.
200 From the clone trajectories, we calculated the mean clone velocity at different positions along the AP
201 axis (Figure 2K and see Materials and methods). Clones initially located 800 μm anterior to the

202 amputation plane translocate slowly, with a velocity of $20 \pm 9 \mu\text{m/day}$. In contrast, the more posterior a
 203 clone is, the faster it translocates.

204 **Cell proliferation drives the outgrowth of the regenerating spinal cord**

205 The fact that cell density along the AP axis is constant in space and time (Figure 2B-C), made
 206 us reason that the spinal cord must grow as a result of increasing cell numbers. In line with this, we
 207 found a high-proliferation zone, first spanning from $800 \mu\text{m}$ anterior to the amputation plane, and
 208 showed that the increase in cell proliferation is due to both (i) the acceleration of the cell cycle and (ii)
 209 the activation of quiescent stem cells (Figure 2D-H). The influx of cells that we identified could also
 210 contribute to increasing cell numbers in the regenerating spinal cord (Figure 2I-K). To assess the
 211 contribution of these cellular mechanisms to the outgrowth time-course, we used a quantitative
 212 mathematical modeling framework (Greulich & Simons 2016; Rué & Martinez Arias, 2015; Oates *et al.*,
 213 2009). We formalized the influence of each cellular mechanism on the total number of proliferative and
 214 quiescent SOX2⁺ cells in the high-proliferation zone in a mathematical model of cell numbers (Figure
 215 3A, see Materials and methods, equations (3) and (4)). As cell density along the AP axis is constant,
 216 the cell number is proportional to the AP length of the growing high-proliferation zone. Hence, we can
 217 transform the model of cell numbers into an equivalent model for the tissue geometry that predicts the
 218 spinal cord outgrowth, L , and growth fraction, GF :

$$\frac{dL}{dt} = \frac{\text{divisions of proliferative cells}}{r(t) (L + L_0) GF} + \frac{\text{influx of cells into the high-proliferation zone}}{\bar{v}}, \quad L(t = 0) = 0, \quad (1)$$

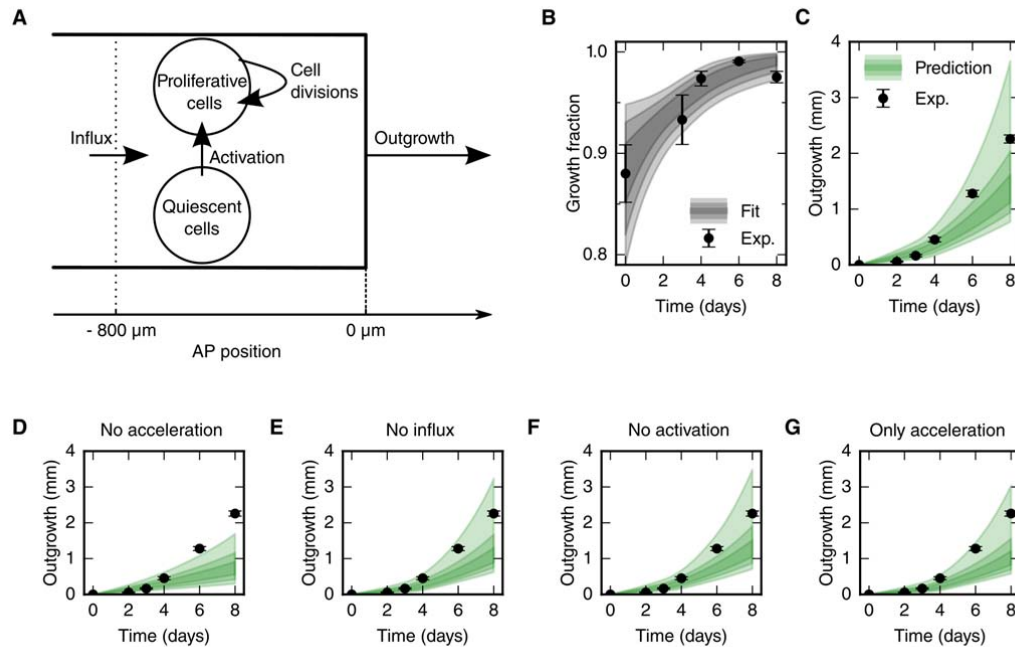
$$\frac{dGF}{dt} = \frac{\text{activation of quiescent cells}}{(1 - GF) k} + \frac{\text{dilution of quiescent cells in the expanding pool of proliferative cells}}{(1 - GF) r(t) GF}, \quad GF(t = 0) = GF_0, \quad (2)$$

219 where $L_0 = 800 \mu\text{m}$ is the length of the high-proliferation zone, GF_0 is the growth fraction in
 220 uninjured tails, $r(t)$ is the proliferation rate at time t , v is the velocity of cells $800 \mu\text{m}$ anterior to the
 221 amputation plane, and k is the cell cycle entry rate. As we determined the proliferation rate time-
 222 course $r(t)$ (Figure 2G), the initial growth fraction GF_0 (Figure 2F) and the influx velocity v (Figure 2K),
 223 only the cell cycle entry rate k is unknown. By fitting the model to the experimental growth fraction data
 224 from day 0 to day 6 (Figure 3B), we determined this parameter as $k = 0.2 \pm 0.1 \text{ day}^{-1}$. Strikingly, the
 225 model predicts a spinal cord outgrowth time-course that recapitulates the observed experimental data
 226 (Figure 3C). This fit-free agreement shows that the acceleration of the cell cycle, the activation of

227 quiescent neural stem cells, and an influx of cells into the regenerate quantitatively explain the
228 observed spinal cord outgrowth.

229 To quantitatively determine the contribution of each cellular mechanism to the regenerative
230 spinal cord outgrowth, we switched them off one by one *in silico*. First, we switched off the
231 acceleration of the cell cycle, modeling growth only with basal cell proliferation, the influx of cells, and
232 the activation of quiescent neural stem cells (Figure 3D). This predicted a maximum outgrowth of
233 1.7 mm ($p = 0.003$) which is 0.6 mm shorter than the observed outgrowth at day 8. This result shows
234 that the acceleration of the cell cycle is a key driver of regenerative spinal cord outgrowth. In contrast,
235 switching off cell influx (Figure 3E) or the activation of quiescent neural stem cells (Figure 3F) has
236 almost no effect on the predicted outgrowth, which suggests that these cellular mechanisms are not
237 major drivers of regenerative spinal cord outgrowth. Indeed, even when we switched off both cell influx
238 and cell activation the observed outgrowth time-course is in agreement with the model prediction
239 (Figure 3G). Together, these results show that the acceleration of the cell cycle in cells that were
240 already proliferating in the uninjured spinal cord can explain the observed spinal cord outgrowth during
241 regeneration.

242 To test the prediction of our model against an independent experimental dataset, we revisited
243 data of *Sox2*-knockout spinal cords (Fei *et al.*, 2014). Fei and colleagues found evidences that *Sox2*-
244 knockout prevented the acceleration of the cell cycle during regeneration and lead to shorter spinal
245 cord outgrowth. In agreement with these findings, running our model with the acceleration of the cell
246 cycle switched off recapitulated the shorter outgrowth in the *Sox2*-knockout condition (Figure 3 – figure
247 supplement 2 and see Materials and methods).



248
249

250 **Figure 3. Mechanistic model of spinal cord outgrowth.** (A) Sketch of cellular mechanisms included in the
 251 model: cell proliferation, quiescent cell activation, and cell influx into the 800 μm high-proliferation zone. (B)
 252 Growth fraction time-course of the SOX2^+ cell population in the high-proliferation zone as observed (black dots)
 253 and fitted by the model (gray shaded areas, from darker to lighter, 68%, 95% and 99.7% confidence intervals of
 254 the model prediction). (C) Spinal cord outgrowth during the first eight days of regeneration as observed (black
 255 dots, $n = 8$ axolotls) and predicted by the model (equations (1) and (2)) (green shaded areas, from darker to
 256 lighter, 68%, 95% and 99.7% credibility intervals). The model prediction is in agreement with the experimental
 257 data. (D-G) Prediction of spinal cord outgrowth for four model scenarios based on equations (1) and (2) with
 258 selected mechanisms switched off (green shaded areas). Black dots show the same experimental data as in
 259 panel (C). (D) The acceleration of the cell cycle is switched off. Hence, the proliferation rate is fixed to the basal
 260 proliferation rate of uninjured animals. (E) Cell influx is switched off ($v = 0$). (F) Quiescent cell activation is
 261 switched off ($k = 0$). (G) Cell influx and quiescent cell activation are switched off ($k = 0, v = 0$). Corresponding
 262 predictions for growth fraction in Figure 3 – figure supplement 1.

263 Discussion

264 The spinal cord tissue size and architecture is faithfully restored after tail amputation in
 265 axolotls. This unique regenerative capability relies on neural stem cells surrounding the central canal
 266 of the spinal cord. These cells re-activate an embryonic-like gene expression program that implements
 267 PCP signaling to make possible the increase in cell proliferation while maintaining a tube-like structure

268 (Rodrigo Albors *et al.*, 2015). However, the precise contribution of proliferation-based mechanisms to
269 the outgrowth of the regenerated spinal cord and whether other cellular mechanisms are involved
270 remained unknown.

271 Here, we combined detailed quantitative datasets with mathematical modeling to dissect the
272 cellular mechanisms that underlie regenerative spinal cord outgrowth in axolotls. We found that the
273 response to injury involves (i) changes in the cell proliferation rate, (ii) activation of quiescent neural
274 stem cells, and (iii) cell influx into the regenerating spinal cord, while maintaining a surprisingly
275 organized neural stem cell-scaffold. Modeling the contribution of each of these mechanisms to tissue
276 outgrowth upon regeneration, we uncovered that the acceleration of the cell cycle is the main driver of
277 regenerative spinal cord outgrowth in axolotls.

278 Increased proliferation of SOX2⁺ cells upon spinal cord injury is a common feature among
279 vertebrates (Becker & Becker, 2015). In zebrafish (Hui *et al.*, 2010; Hui *et al.*, 2015), *Xenopus* (Gaete
280 *et al.*, 2012), mouse (Lacroix *et al.*, 2014) and axolotl (this work, Rodrigo Albors *et al.* 2015, Holtzer,
281 1956) traumatic spinal cord injury triggers a long-range wave of increased cell proliferation. It is
282 however clear that although the potential to replace lost cells or tissue exists in other species, they are
283 not as efficient as axolotls at resolving spinal cord injuries. A more comprehensive characterization of
284 cell proliferation responses is thus needed to understand fundamental differences between species
285 with different regenerative capabilities. In our previous study, we uncovered that spinal cord stem cells
286 in the axolotl speed up their cell cycle during regeneration (Rodrigo Albors *et al.*, 2015). Performing
287 detailed quantifications, we were now able to delineate a high-proliferation zone that initially spans
288 from the 800 μm adjacent to the amputation plane to the regenerating tip, and later shifts posteriorly
289 as the spinal cord regrows. Although some quiescent neural stem cells enter the cell cycle during
290 regeneration, we demonstrate that the observed increase in proliferation is primarily due to the
291 acceleration of the cell cycle within the regenerating neural stem cell pool. By performing experiments
292 *in silico* using our mechanistic model of spinal cord regeneration, we demonstrate that the acceleration
293 of the cell cycle can explain the observed spinal cord outgrowth.

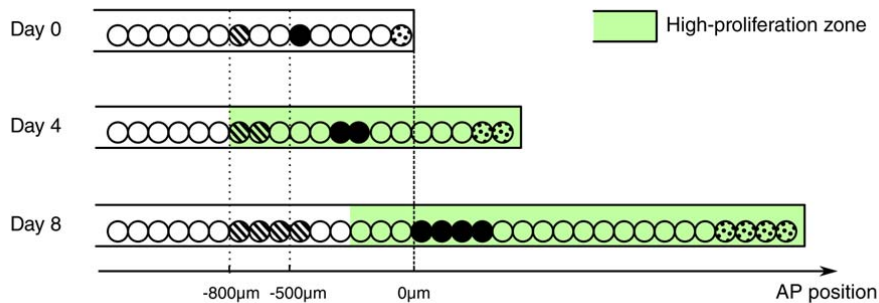
294 We further applied our model to an independent experimental dataset in which *Sox2*-knockout
295 spinal cords do not regrow properly upon amputation, due to the inability of *Sox2*-knockout cells to
296 'change gears' in response to injury (Fei *et al.*, 2014). Indeed, *Sox2*-knockout cells express PCNA and
297 are in theory able to proliferate, but their lower incorporation of the thymidine analog 5-ethynyl-2'-

298 deoxyuridine (EdU) suggests that they cannot speed up the cell cycle (Fei *et al.*, 2014). We were able
299 to show that the reduced outgrowth in *Sox2*-knockout spinal cords can be quantitatively explained by
300 the lack of cell cycle acceleration (Figure 3 – figure supplement 2). However, it is important to point out
301 that our model does not include the regulation of individual cellular mechanisms and thus it does not
302 consider compensatory mechanisms that may operate under perturbed conditions. To apply our model
303 to the *Sox2*-knockout dataset, we assumed that knocking out *Sox2* only affects the acceleration of the
304 cell cycle. The fact that the model successfully recapitulated the experimental outgrowth in the *Sox2*-
305 knockout scenario suggests that compensatory mechanisms might have a small contribution in this
306 condition. Nevertheless, the validity of this assumption remains to be further investigated.

307 Our approach and findings highlight the importance of mathematical modeling and careful
308 quantification of cellular mechanisms to understand the mechanisms of regeneration. Moreover, our
309 detailed spatial and temporal characterization of cell proliferation may help to focus the search for key
310 signals that might be operating in the high-proliferation zone to speed up the cell cycle of regenerative
311 neural stem cells. It will be interesting to see whether the expression of AxMLP, the recently identified
312 regeneration-initiating factor in axolotls (Sugiura *et al.*, 2016), correlates in time and space with the
313 high-proliferation zone. This work thus provides a deeper understanding of spinal cord regeneration in
314 axolotls and new insights to help elucidating the molecular mechanisms that drive spontaneous spinal
315 cord regeneration *in vivo*.

316 Besides the increase in cell proliferation, we uncovered an influx of cells into the regenerating
317 spinal cord. Cells move along the AP axis of the spinal cord but maintain their relative position: cells
318 translocate faster the closer they are to the amputation plane (Figure 2J,K). In line with earlier work
319 (Mchedlishvili *et al.*, 2007), we found that cells initially located within the 500 μm anterior to the
320 amputation plane contribute to the regenerated spinal cord; while cells outside this zone translocate
321 slower, and cells at 800 μm , the border of the high-proliferation zone, almost do not move. This would
322 be consistent with a model in which cells are passively displaced, pushed by more anterior dividing
323 cells. In this model, the more posterior a cell is the more cells anterior to that cell divide and the
324 stronger is the push, making the cell translocate faster (Figure 4). Importantly, the proliferative
325 response extends beyond the 500 μm anterior to the amputation plane that gives rise to the
326 regenerated spinal cord (Mchedlishvili *et al.*, 2007). In the light of this model, it is plausible that cells in
327 the posterior 500 μm of the high-proliferation zone regenerate the spinal cord while cells from the

328 anterior 300 μm of the high-proliferation zone replenish and push out the 500 μm regeneration source
329 zone.



330
331 **Figure 4. Conceptual model of spinal cord growth during regeneration.** Only one row of stem cells is shown
332 as circles and three cell clones are marked with different patterns (striped, black and dotted). In the uninjured
333 spinal cord (Day 0), cells divide at a slow, basal proliferation rate (white background). From day 4 after
334 amputation, cells speed up their cell cycle and the growth fraction increases, within a high-proliferation zone that
335 initially extends 800 μm anterior to the amputation plane (green background). The density of neural stem cells
336 along the spinal cord stays constant and spinal cord outgrowth is achieved by an increase in the total number of
337 neural stem cells. Acceleration of the cell cycle in the high-proliferation zone is the major driver of this increase in
338 cell numbers. Dividing cells might push cells posteriorly. The more posterior a cell is the more cells anterior to that
339 cell divide and push the cell making it move faster: While an anterior clone (striped) hardly moves, clones in the
340 center of the high proliferation zone (black) move faster. Clones that start at the amputation plane (dotted) stay at
341 the tip of the regenerating spinal cord and move fastest.

342

343 A notable finding of this study is that the increase in cell numbers during regeneration is tightly
344 regulated so that the regenerating spinal cord extends while maintaining constant cell density and
345 proper tube-like structure. This tube-like structure made up almost entirely of neural stem cells might
346 be essential to act as a scaffold for rebuilding the spinal cord tissue architecture. Previously, we
347 showed that the activation of PCP signaling within the source zone instructs cells to divide along the
348 growing axis of the spinal cord and is key for effective spinal cord regeneration. This work highlights
349 the importance of orderly and directed expansion of the neural stem cell pool for efficient spinal cord
350 regeneration.

351 Together, our findings provide a quantitative mechanistic understanding of the cellular
352 mechanisms that drive complete spinal cord regeneration in axolotls. By performing a quantitative
353 modeling approach combined with quantitative experimental data, we found that axolotl spinal cord
354 outgrowth is driven by the acceleration of the cell cycle in a pool of SOX2⁺ neural stem cells restricted
355 in space and time. Whether this peculiar spatiotemporal proliferative pattern is unique to the axolotl
356 and how this correlates with injury-induced signals remain to be elucidated.

357 **Materials and methods**

358 **Axolotls**

359 Axolotls, *Ambystoma mexicanum*, from 2 to 3 cm in length snout-to-tail were used for
360 experiments. Axolotls were kept in tap water in individual cups and fed daily with *Artemia*. Before any
361 manipulation or imaging, axolotls were anaesthetized in 0.01% benzocaine. The axolotl animal work
362 was performed under permission granted in animal license number DD24-9168.11-1/2012-13
363 conferred by the Animal Welfare Commission of the State of Saxony, Germany (Landesdirektion
364 Sachsen).

365 **Measurement of spinal cord outgrowth**

366 Images of regenerating tails were acquired on an Olympus SZX16 stereomicroscope using the
367 Cell[^]F software by Olympus. Spinal cord outgrowth was measured from bright field images in Fiji
368 (RRID:SCR_002285). First, the amputation plane which is clearly visible in the myotome was marked
369 with a line. Then, the length between the intersection of the amputation plane with the spinal cord and
370 the spinal cord tip was measured with Fiji's line tool.

371 **Cell count data**

372 The cell count data of SOX2⁺ and SOX2⁺/PCNA⁺ cells per cross section and mitotic cells in
373 50 µm sections were taken from Rodrigo Albors *et al.*, 2015.

374 **Analysis of SOX2⁺ cell count data**

375 To test whether the SOX2⁺ cells per cross section showed a spatial pattern along the AP axis
376 or not, we used three different methods (Figure 2B,B', Figure 2 – figure supplement 1). First, it was
377 tested if the cell count data linearly depends on spatial position along the AP axis using Bayesian
378 inference (see Supplementary notebook "Constant density"). The slope was always smaller than 0.13
379 cells / mm and only significantly different from 0 ($p < 0.05$) for 4 of the 15 replicates. Second, a model
380 of two spatially homogeneous zones was fitted to the data using Bayesian inference (see
381 Supplementary notebook "Constant density"). Here, only 4 of the 15 replicates showed a significant
382 difference in density between the two zones ($p < 0.05$). These first two methods indicated that, for an
383 average animal, there is no significant change of the number of SOX2⁺ cells per cross section along
384 the AP axis. Third, the data was collapsed ignoring the spatial position, and the resulting cell count

385 histogram was tested for being a normal distribution using the SciPy function `scipy.stats.normaltest`
386 (D'agostino, 1971; D'agostino and Pearson, 1973). Only for one of the replicates the null hypothesis
387 could be rejected ($p < 0.05$), hence SOX2⁺ cell density in an average animal was considered spatially
388 homogeneous with Gaussian noise in this study.

389 For each replicate the mean number of SOX2⁺ cells per cross section averaged over all
390 measurements along the AP axis was calculated. To access whether there was a significant change in
391 this mean number, the replicates were grouped according to their time post amputation. A one-way
392 ANOVA-test showed no significant differences among the groups ($p = 0.08$, see Supplementary
393 Notebook "Constant density").

394 **Analysis of proliferation count data**

395 The counts of SOX2⁺ cells, SOX2⁺/PCNA⁺ cells and mitotic cells were analyzed by fitting a
396 mathematical model of two adjacent spatial proliferation zones to the data of each time point (Figure
397 2D,D', Figure 2 – figure supplement 3).

398 The model that predicts the number of SOX2⁺/PCNA⁺ cells per cross section and the number
399 of mitotic cells in three-dimensional (3D) 50 μm sections based on the growth fraction and mitotic
400 index was defined as follows: If the number of SOX2⁺ cells for a specific cross section along the AP
401 axis, N_S , had been measured, it was used for this section. If the data for the specific section was
402 missing, N_S was computed by assuming that there is a constant expected number of SOX2⁺ cells per
403 cross section and that the deviations from the expected value follow a normal distribution. The mean
404 and standard deviation of this normal distribution were estimated by the sample mean and standard
405 deviation of the sample of the measured numbers of SOX2⁺ cells per cross section for each replicate.
406 The number of SOX2⁺ in a cross section is independent from other cross sections. The state
407 'Proliferative', i.e. SOX2⁺/PCNA⁺, is independently assigned to each SOX2⁺ cell with probability p_p or
408 'Quiescent' with probability $1 - p_p$ (Figure 2E). Hence, for a given number of SOX2⁺ cells in a cross
409 section, N_S , the number of SOX2⁺/PCNA⁺ cells per cross section, N_P , follows a binomial distribution
410 with N_S experiments and success probability p_p . Consequently, the expected growth fraction equals p_p .
411 As the number of mitotic cells, N_M , in 3D 50 μm sections was measured previously, we estimated the
412 number of SOX2⁺/PCNA⁺ cells also in a 3D 50 μm section, $N_{PS} = 50 \mu\text{m}/l_{cell} \cdot N_P$, where $l_{cell} = 13.2 \pm$
413 $0.1 \mu\text{m}$ is the mean AP length of SOX2⁺ cells (Rodrigo Albers *et al.*, 2015). Assuming that the cell
414 cycle position and hence the cell cycle phase of each cell is independent of all other cells, the state

415 ‘Proliferative, mitotic’ is independently assigned to each SOX2⁺/PCNA⁺ cell with probability p_m or
416 ‘Proliferative, non-mitotic’ with probability $1 - p_m$. Hence, the number of mitotic cells per section, N_M ,
417 follows a binomial distribution with N_{PS} experiments and success probability p_m . Consequently, the
418 expected mitotic index equals p_m . For given values of p_p and p_m the model gives a likelihood for the
419 observed number of SOX2⁺/PCNA⁺ cells per cross section and mitotic cells per 3D section that can be
420 used to fit the model parameters. To reflect the assumption of two spatial proliferation zones, p_p and
421 p_m have spatial dependencies in the form of step functions (Figure 2E’). Hence, there can be different
422 growth fractions and mitotic indices for the anterior and the posterior zone, respectively. The spatial
423 position of the border between the zones is another model parameter termed *switchpoint*.
424 Furthermore, variability between replicates in the switchpoint is modeled as a normal distribution with
425 standard deviation σ_{switch} . Likewise, variability in growth fraction and mitotic index between replicates
426 is modeled with a normal distribution with spatially homogeneous standard deviations σ_{GF} and σ_{mi} ,
427 respectively. Hence, the resulting model to describe the cell count data of all replicates at a given time
428 point has 8 parameters: the switchpoint, growth fraction and mitotic index in the anterior zone and in
429 the posterior zone, respectively, and the inter-replicate variabilities σ_{switch} , σ_{GF} and σ_{mi} . Those
430 parameters were estimated with Bayesian inference using uniform priors for uninjured animals and at
431 3, 4, 6 and 8 days. Fitting was performed using a Markov chain Monte Carlo algorithm implemented in
432 pymc (Figure 2F-F”, Figure 2 – figure supplement 4, see also Supplementary notebook
433 “step_model_fixed_density_fit_per_timepoint”). To verify the fitting procedure, test data were created
434 by simulating our model with picked parameter values. These “true” parameter values were then
435 found to be included in the 95% credibility intervals of the parameter values inferred from the test data
436 with our fitting procedure.

437 **Proliferation rate time-course**

438 The cell cycle length at day 6 was estimated previously using a cumulative 5-bromo-2'-
439 deoxyuridine (BrdU) labelling approach (Rodrigo Albors *et al.*, 2015). For the sake of consistent
440 methodology within the present study, the data were reanalyzed with bootstrapping using case
441 resampling (see Supplementary Notebook “brdu_bootstrapping_day6”). In agreement with the
442 previous analysis the cell cycle length was estimated as 117 ± 12 h corresponding to a proliferation
443 rate of 0.21 ± 0.02 per day at 6 days after amputation.

444 As the mitotic index is proportional to the proliferation rate (Smith & Dendy, 1962), the mitotic
445 index time-course in the high-proliferation zone was rescaled with the proliferation rate at day 6 to
446 obtain the proliferation rate time-course:

$$r(t) = \frac{mi(t)}{mi(day\ 6)} r(day\ 6),$$

447 where $r(t)$ is the proliferation rate at time t , and mi is the mitotic index. The mitotic index in the
448 high-proliferation zone was estimated as described in (Rodrigo Albors *et al.*, 2015).

449 **Axolotl spinal cord electroporation**

450 Axolotl larvae (2 cm snout-to-tail) were electroporated with a dual fluorescent reporter plasmid
451 (cytoplasmic eGFP and nuclear Cherry). Cells were electroporated by cutting the tail of 2 cm-long
452 larval axolotls and inserting a DNA-filled electrode into the spinal cord (Echeverri & Tanaka 2003). To
453 transfect DNA into only a few cells, optimum electroporation conditions were three pulses of 50 V, 200
454 Hz and a length of 100 ms, applied using an SD9 Stimulator (Grass Telefactor, West Warwick, RI).

455 ***In vivo* imaging of labeled cells in the spinal cord**

456 Axolotls with sparsely labelled cells in the spinal cord were amputated, leaving cells at
457 different distances from the amputation plane. Regenerating axolotls were anaesthetized and imaged
458 every 1-2 days by placing them on a cover slip. Labelled cells were imaged using a Zeiss Apotome A1
459 microscope.

460 **Clone tracking**

461 The distance between the amputation plane and the anterior border of a clone was measured
462 manually in each image using AxioVision microscopy software (RRID:SCR_002677). Representative
463 images of one axolotl showing a clone at different distances from the amputation plane during
464 regeneration time are shown in Figure 2I. All the individual images are in Supplementary file 2.

465 **Clone velocity**

466 To estimate the mean velocity of clones at different spatial positions, the space along the AP
467 axis was subdivided into 800 μm bins. For each clone trajectory, the position measurements were
468 grouped according to these bins. Groups containing less than 2 measurements were excluded. The
469 average clone velocity for each group was estimated with linear regression. Then, the mean and
470 standard deviation of the velocity of all the clones in a bin was calculated (see Supplementary
471 Notebook "clone_velocities").

472 **Estimation of the total number of quiescent cells in the high-proliferation zone**

473 The total number of quiescent cells in the high-proliferation zone, $N_q(t)$, was estimated by
 474 $N_q(t) = N_q^s \cdot L(t)/l_{cell}$, where N_q^s is the mean number of SOX2⁺/PCNA⁻ cells per cross section, l_{cell} is
 475 the mean AP cell length, and $L(t)$ is the outgrowth time-course.

476 **Mechanistic model of spinal cord outgrowth**

477 To simultaneously evaluate the importance of cell proliferation, cell influx and activation of
 478 quiescent cells in the outgrowth of the spinal cord we performed a data-driven modeling approach
 479 (Greulich & Simons 2016; Rué & Martinez Arias, 2015; Oates *et al.*, 2009). This approach allows to
 480 establish causal relationship between the individually quantified cellular processes and it has been
 481 previously employed to unravel the stem cell dynamics during spinal cord development in chick and
 482 mouse (Kicheva *et al.*, 2014). Although less frequent so far, modeling is more and more being used in
 483 the regeneration arena (Durant *et al.*, 2016; for an overview see Chara *et al.*, 2014). In this study we
 484 model the number of proliferative and quiescent cells in the high-proliferation zone by the following
 485 ordinary differential equations (Figure 3A):

$$\frac{dN_p}{dt} = \overbrace{r(t) N_p}^{\text{cell divisions}} + \overbrace{k N_q}^{\text{activation}} + \overbrace{\frac{N_p}{N_p + N_q} v \rho}^{\text{influx}}, \quad N_p(t=0) = N_p^0 \quad (3)$$

$$\frac{dN_q}{dt} = - k N_q + \frac{N_q}{N_p + N_q} v \rho, \quad N_q(t=0) = N_q^0 \quad (4)$$

486 where N_p^0 and N_q^0 are the initial cell numbers in this zone, $r(t)$ is the proliferation rate at time t ,
 487 v is the velocity of cells 800 μm anterior to the amputation plane, ρ is the density of neural stem cells
 488 along the AP axis and k is the quiescent cell activation rate. The factors $N_{p/q} / (N_p + N_q)$ ensure that the
 489 influx of cells into the high-proliferation zone does not alter the growth fraction. As the density is
 490 constant one can write

$$\rho \cdot (L + L_0) = N_p + N_q, \quad (5)$$

491 where L is the outgrowth posterior to the amputation plane and $L_0 = 800 \mu\text{m}$ is the high-
 492 proliferation zone length at $t = 0$. Using this relation and the definition of the growth fraction GF ,

$$GF = \frac{N_p}{N_p + N_q}, \quad (6)$$

493 the cell number model was reformulated as a model for outgrowth and growth fraction (see
 494 Results, equations (1) and (2)).

495 The assumption that the population mean model parameters can be used to estimate the
496 population mean outgrowth time-course was used when simulating the model and interpreting results.
497 The confidence intervals of the model prediction were estimated with a Monte Carlo approach using
498 bootstrapping with a case resampling scheme (100,000 iterations). In each iteration we case-
499 resampled the cell count data, the BrdU incorporation data and the clone trajectory data, and
500 calculated the proliferation rate time-course, clone velocity at -800 μm and initial growth fraction from
501 this resampled data as described above. Then, in each iteration, these bootstrapped parameter values
502 were used to estimate the activation rate k by fitting the model prediction of the growth fraction to the
503 data (Figure 3B). The growth fraction measurement of day 8 was excluded from the fit because its
504 precise value would only affect the model prediction after this day. Now, as all parameters were
505 estimated, an outgrowth trajectory was calculated for each iteration. This ensemble of trajectories was
506 used to calculate the confidence intervals of the model prediction (Figure 3C). The same approach
507 was used for the model scenarios with individual cellular mechanisms turned off (Figure 3D-G). The
508 source code is available in the Supplementary notebook "lg_model".

509 **Validation of a model prediction against an experimental dataset**

510 Control animals by Fei et al., 2014 showed less regenerative outgrowth than our 'normally'
511 regenerating animals. This could be either due to their control CRISPR treatment or due to their
512 reduced feeding. To account for the reduced growth, we assumed that all cellular mechanisms
513 maintain the same relative contribution in Fei and colleagues' control as they have in normal
514 regeneration. This assumption allowed linear rescaling of the outgrowth dataset from Fei and
515 colleagues to match our 'normal' outgrowth dataset (Figure 3 – figure supplement 2A, Supplementary
516 notebook "lg_model"). We also assumed that Sox2-knockout only affects the acceleration of the cell
517 cycle but that all other cellular mechanisms remain unaffected (i.e. compensatory mechanisms are not
518 considered). Fewer neural stem cells make up the circumference of Sox2-knockout spinal cords (Fei
519 et al., 2014). Assuming that AP cell length is unchanged this means that cell density is decreased in
520 this condition. Therefore, we corrected the outgrowth for the Sox2-knockout dataset to a density
521 corrected outgrowth by $L_{corr} = N_S^{Sox2^{ko}} / N_S^{control} \cdot L$, where L_{corr} is the density corrected outgrowth, L is
522 the measured outgrowth in the Sox2-knockout dataset and $N_S^{Sox2^{ko}}$ and $N_S^{control}$ are the mean number
523 of neural stem cells per cross section in the Sox2-knockout and control condition, respectively (Figure
524 3 – figure supplement 2B, Supplementary notebook "lg_model").

525 **Coordinate system**

526 Time starts with the event of amputation. For spatial positions along the AP axis of the spinal
527 cord, the amputation plane defines 0; positive values refer to positions posterior to the amputation
528 plane, in regenerated tissue; negative values refer to positions anterior to the amputation plane. In all
529 images, anterior is to the left.

530 **Statistics and computational tools**

531 If not stated otherwise, measurements are reported as mean \pm standard error of the mean. In
532 the figures * denotes $p < 0.05$ and ** denotes $p < 0.01$ for the respective test as indicated in the figure
533 caption.

534 Image analysis was performed with Fiji (Schindelin *et al.*, 2012) and AxioVision Microscopy
535 software (Zeiss). Data analysis was performed using the python modules bokeh
536 (<http://bokeh.pydata.org>), iminuit (<http://github.com/iminuit/iminuit>), ipycache
537 (<http://github.com/rossant/ipycache>), Jupyter Notebook (<http://jupyter.org/>), matplotlib (Hunter, 2007),
538 numba (<http://numba.pydata.org/>), pandas (McKinney, 2010), probfit (<http://github.com/iminuit/probfit>),
539 pymc (Patil *et al.*, 2010), SciPy (Jones *et al.*, 2001) and uncertainties
540 (<http://pythonhosted.org/uncertainties/>).

541 **Supplementary notebooks**

542 Jupyter Notebooks containing the source code for all computations performed together with
543 the data and referred to as individually named Supplementary notebooks in this work can be found
544 under <https://doi.org/10.5281/zenodo.160333>.

545 **Acknowledgements**

546 We are grateful to Beate Gruhl, Sabine Mögel, Anja Wagner, and Heino Andreas for
547 outstanding axolotl care. We thank Walter de Back, Nuno Barros, Emanuel Cura Costa, Ji-Feng Fei,
548 Keisuke Ishihara, Jörn Starruß and Anja Voß-Böhme for helpful discussions.

549 **Competing interests**

550 The authors declare no competing interests.

551 **Author contributions**

552 FR, Conception and design, Analysis and interpretation of data, Drafting or revising the article.
553 ARA, Conception and design, Acquisition of data, Analysis and interpretation of data, Drafting or
554 revising the article.
555 VM, Acquisition of data, Drafting or revising the article.
556 LB, Analysis and interpretation of data, Drafting or revising the article.
557 AD, Analysis and interpretation of data, Drafting or revising the article.
558 EMT, Conception and design, Analysis and interpretation of data, Drafting or revising the article.
559 OC, Conception and design, Analysis and interpretation of data, Drafting or revising the article.

560 **Funding**

561 This work was supported by grants from the Human Frontier Science Program (HFSP)
562 RGP0016/2010, DFG-274/2-3/SFB655 'Cells into tissues', TU Dresden Graduate Academy
563 (great!lipid4all), the Center for Regenerative Therapies to E.M.T. and Agencia Nacional de Promoción
564 Científica y Tecnológica (ANPCyT) PICT-2014-3469 'Mecanismos de Regeneración de la médula
565 espinal del Axolotl: Una aproximación de Biología de Sistemas' to O.C. and BMBF grant (0316169A)
566 to L.B. A.R.A. was funded by a DIGS-BB fellowship; F.R. and O.C. were funded by the HFSP, the
567 German Ministry for Education and Research (BMBF) and TU Dresden Graduate Academy
568 (great!lipid4all). O.C. is a career researcher from Consejo Nacional de Investigaciones Científicas y
569 Técnicas (CONICET) of Argentina.

570 **References**

571 Becker CG, Becker T. 2015. Neuronal regeneration from ependymo-radial glial cells: cook, little Pot,
572 cook! *Dev Cell*. **32**(4): 516-527. doi: 10.1016/j.devcel.2015.01.001.
573 Chara O, Tanaka EM, Brusch L. 2014. Mathematical modeling of regenerative processes. *Curr Top*
574 *Dev Biol*. **108**: 283-317. doi: 10.1016/B978-0-12-391498-9.00011-5.
575 D'agostino R, Pearson ES. 1973. Tests for departure from normality. Empirical results for the
576 distributions of b_2 and $\sqrt{b_1}$. *Biometrika* **60**: 613–622. doi: 10.1093/biomet/60.3.613.
577 D'agostino RB. 1971. An omnibus test of normality for moderate and large size samples. *Biometrika*
578 **58**: 341–348. doi: 10.1093/biomet/58.2.341.
579 Durant F, Lobo D, Hammelman J, Levin M. 2016. Physiological controls of large-scale patterning in
580 planarian regeneration: a molecular and computational perspective on growth and form. *Regeneration*.
581 **3**(2): 78-102. doi: 10.1002/reg2.54.

582 Echeverri K, Tanaka EM. 2003. Electroporation as a tool to study in vivo spinal cord regeneration. *Dev*
583 *Dyn.* **226**(2): 418-25. doi: 10.1002/dvdy.10238.

584 Fei JF, Schuez M, Tazaki A, Taniguchi Y, Roensch K, Tanaka EM. 2014. CRISPR-mediated genomic
585 deletion of Sox2 in the axolotl shows a requirement in spinal cord neural stem cell amplification during
586 tail regeneration. *Stem Cell Reports.* **3**(3): 444-59. doi: 10.1016/j.stemcr.2014.06.018.

587 Gaete M, Muñoz R, Sánchez N, Tampe R, Moreno M, Contreras EG, Lee-Liu D, Larraín J. 2012.
588 Spinal cord regeneration in *Xenopus* tadpoles proceeds through activation of Sox2-positive cells.
589 *Neural Dev.* **7**:13. doi: 10.1186/1749-8104-7-13.

590 Greulich P, Simons BD. 2016. Dynamic heterogeneity as a strategy of stem cell self-renewal. *Proc*
591 *Natl Acad Sci U S A.* **113**(27): 7509-14. doi: 10.1073/pnas.1602779113.

592 Holtzer SW. 1956. The inductive activity of the spinal cord in urodele tail regeneration. *J Morphol.* **99**:
593 1-39. doi: 10.1002/jmor.1050990102.

594 Hui SP, Dutta A, Ghosh S. 2010. Cellular response after crush injury in adult zebrafish spinal cord.
595 *Dev Dyn.* **239**(11): 2962-79. doi: 10.1002/dvdy.22438.

596 Hui SP, Nag TC, Ghosh S. 2015. Characterization of proliferating neural progenitors after spinal cord
597 injury in adult zebrafish. *PLoS One.* **10**(12): e0143595. doi: 10.1371/journal.pone.0143595.

598 Hunter JD. 2007. Matplotlib: A 2D Graphics environment. *Comput Sci Eng.* **9**: 90–95. doi:
599 10.1109/MCSE.2007.55.

600 Jones E, Oliphant T, Peterson P *et al.*, 2001. *SciPy: Open source scientific tools for Python.*
601 <http://www.scipy.org/>

602 Kicheva A, Bollenbach T, Ribeiro A, Valle HP, Lovell-Badge R, Episkopou V, Briscoe J. 2014.
603 Coordination of progenitor specification and growth in mouse and chick spinal cord. *Science.*
604 **345**(6204): 1254927. doi: 10.1126/science.1254927.

605 Lacroix S, Hamilton LK, Vaugeois A, Beaudoin S, Breault-Dugas C, Pineau I, Lévesque SA, Grégoire
606 CA, Fernandes KJ. 2014. Central canal ependymal cells proliferate extensively in response to
607 traumatic spinal cord injury but not demyelinating lesions. *PLoS One.* **9**(1):e85916. doi:
608 10.1371/journal.pone.0085916.

609 Mchedlishvili L, Epperlein HH, Telzerow A, Tanaka EM. 2007. A clonal analysis of neural progenitors
610 during axolotl spinal cord regeneration reveals evidence for both spatially restricted and multipotent
611 progenitors. *Development.* **134**(11): 2083-93. doi: 10.1242/dev.02852.

612 McKinney W. 2010. Data structures for statistical computing in Python. In: van der Walt S & Millman J,
613 editors. *Proceedings of the 9th Python in Science Conference.* p. 51–56.

614 Oates AC, Gorfinkiel N, González-Gaitán M, Heisenberg CP. 2009. Quantitative approaches in
615 developmental biology. *Nat Rev Genet.* **10**(8): 517-30. doi: 10.1038/nrg2548.

616 Patil A, Huard D, Fonnesbeck CJ. 2010. PyMC: Bayesian stochastic modelling in Python. *J Stat Softw.*
617 **35**: 1–81. doi: 10.18637/jss.v035.i04.

618 Rodrigo Albors A, Tazaki A, Rost F, Nowoshilow S, Chara O, Tanaka EM. 2015. Planar cell polarity-
619 mediated induction of neural stem cell expansion during axolotl spinal cord regeneration. *eLife*
620 e10230. doi: 10.7554/eLife.10230.

621 Rué P, Martinez Arias A. 2015. Cell dynamics and gene expression control in tissue homeostasis and
622 development. *Mol Syst Biol.* **11**(1):792. doi: 10.15252/msb.20145549.

623 Schindelin J, Arganda-Carreras I, Frise E., Kaynig V, Longair M, Pietzsch T, Preibisch S, Rueden C,
624 Saalfeld S, Schmid B, Tinevez JY, White DJ, Hartenstein V, Eliceiri K, Tomancak P, Cardona A. 2012.
625 Fiji: an open-source platform for biological-image analysis. *Nat Methods.* **9**: 676–682. doi:
626 10.1038/nmeth.2019.

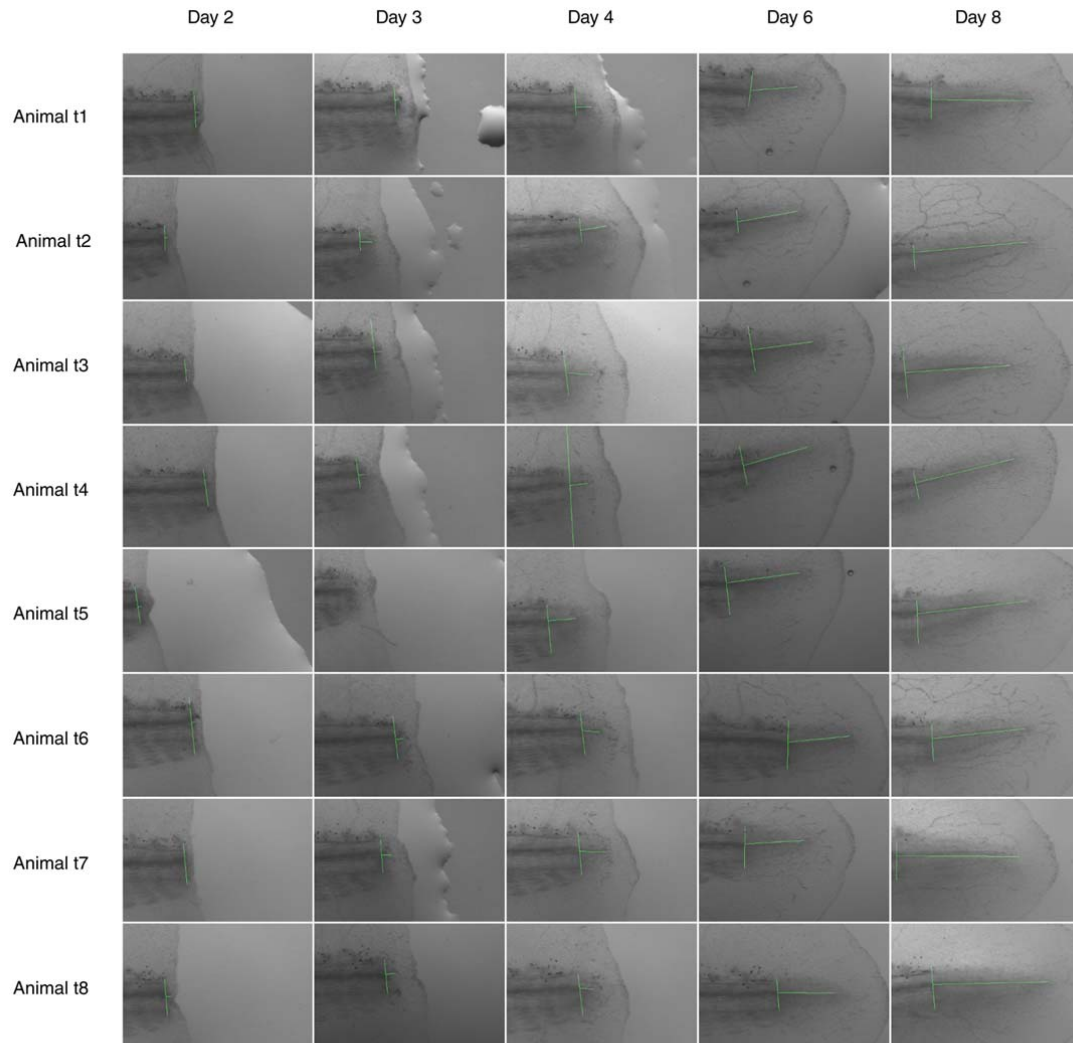
627 Smith C, Dendy PP. 1962. Relation between mitotic index, duration of mitosis, generation time and
628 fraction of dividing cells in a cell population. *Nature* **193**: 555–556. doi: 10.1038/193555a0.

629 Sugiura T, Wang H, Barsacchi R, Simon A, Tanaka EM. 2016. MARCKS-like protein is an initiating
630 molecule in axolotl appendage regeneration. *Nature.* **531**(7593): 237-40. doi: 10.1038/nature16974.

631 Tanaka EM, Ferretti P. 2009. Considering the evolution of regeneration in the central nervous system.
632 *Nat Rev Neurosci.* **10**(10): 713-23. doi: 10.1038/nrn2707.

633 **Figure supplements**

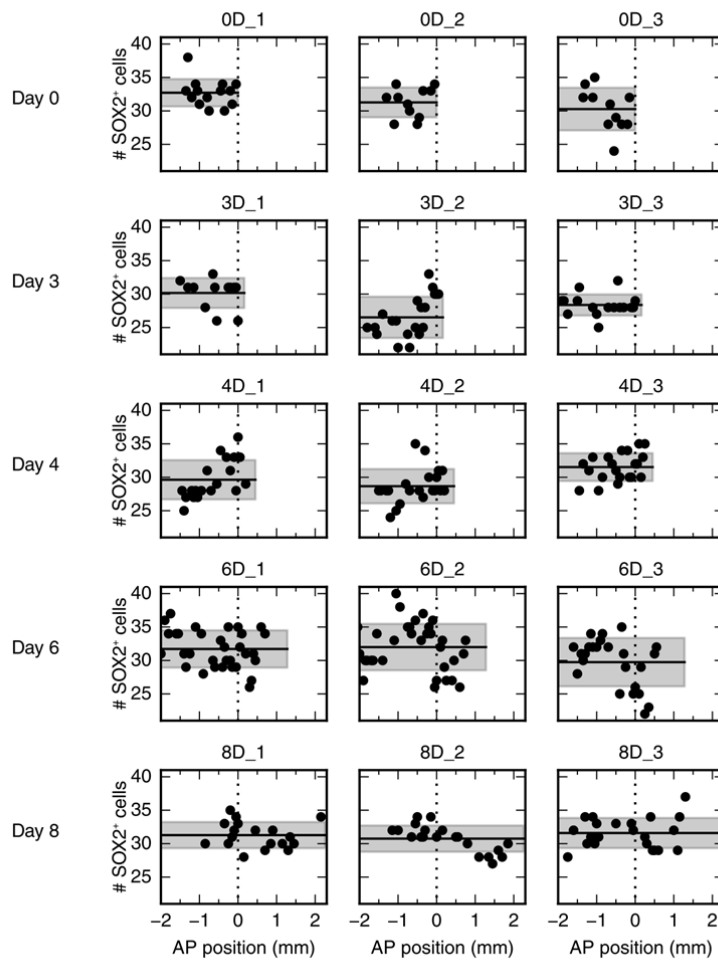
634 **Figure 1 – figure supplement 1**



635

636 **Figure 1 – figure supplement 1.** Images used for spinal cord outgrowth measurements in Figure 1B. Each row
637 shows images from an axolotl; each column shows animals from one time point analyzed. Vertical and horizontal
638 lines mark the amputation plane and the spinal cord outgrowth, respectively. High-resolution images are in
639 Supplementary file 1. Animal t3 is shown in the representative images of Figure 1A.

640 **Figure 2 – figure supplement 1**



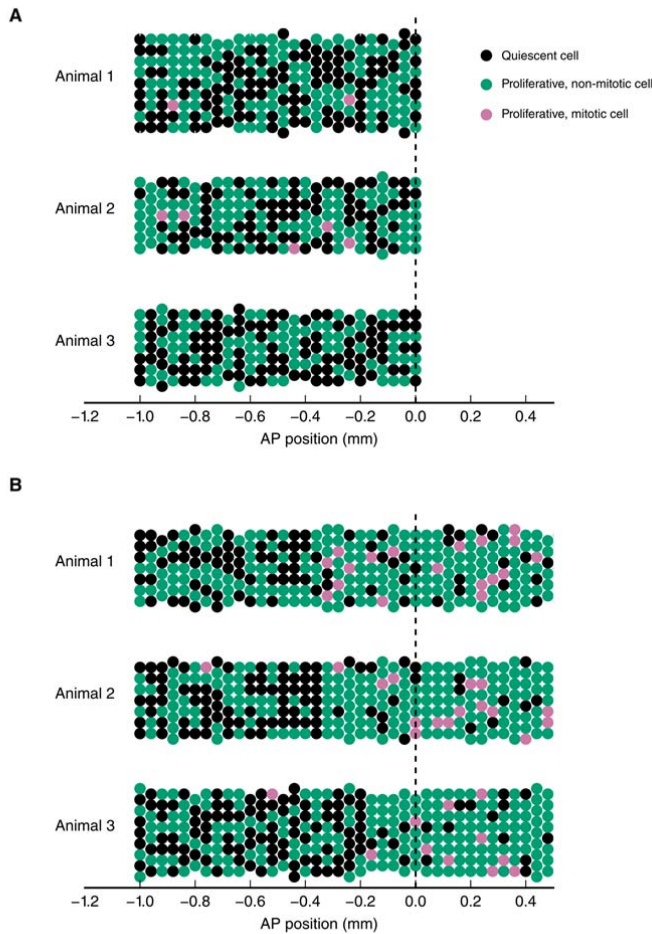
641

642 **Figure 2 – figure supplement 1.** Number of SOX2⁺ cells per cross section along the AP axis for all 15 animals.

643 Each row shows data from three animals at a given time point. Data from animals 0D_1 and 4D_3 are shown as

644 representative data in Figure 2B and B', respectively.

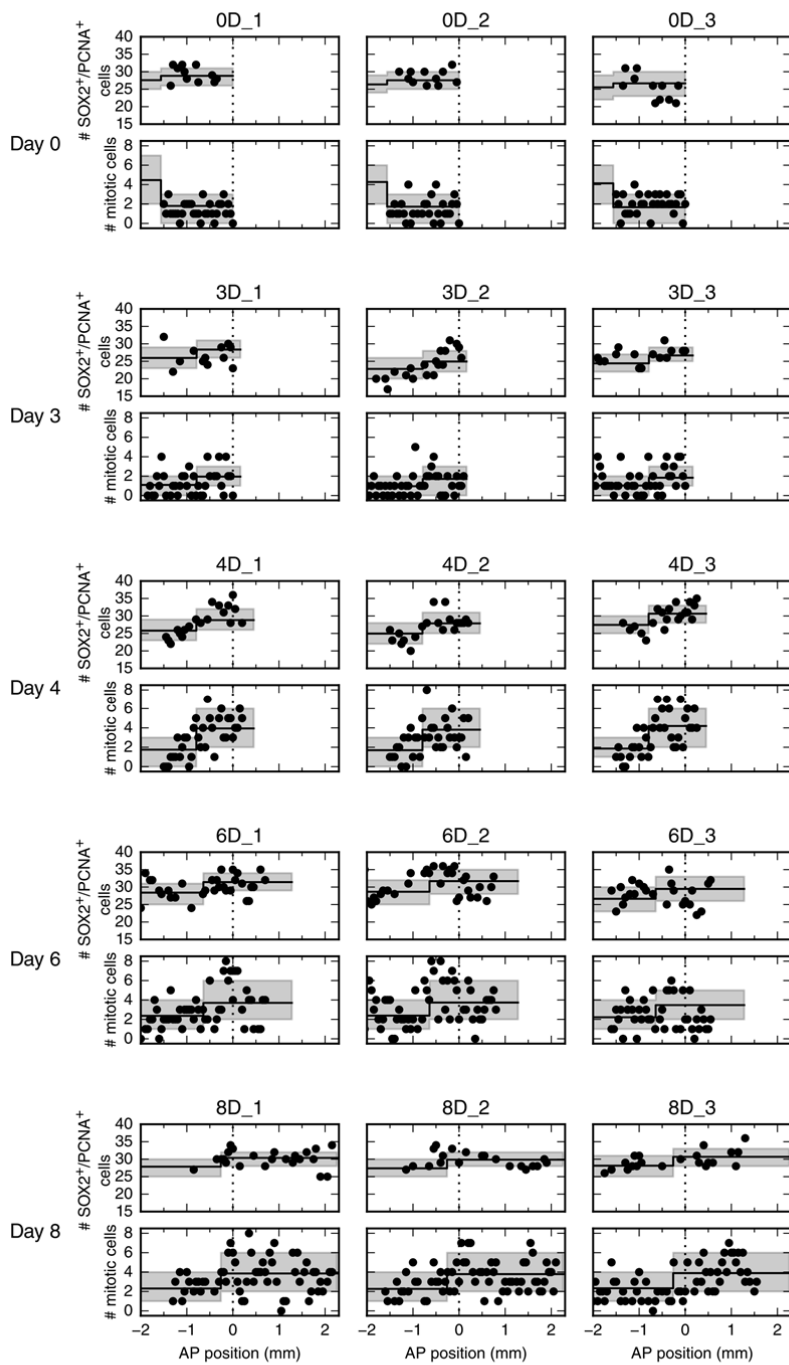
645 **Figure 2 – figure supplement 2**



646

647 **Figure 2 – figure supplement 2.** Simulation of the spatial model of cell counts to analyze the spatiotemporal
 648 pattern of cell proliferation. (A) Simulations of a spatially homogeneous zone of proliferation for 3 animals.
 649 Population mean number of stem cells per cross section, $NS_{pop} = 7$, inter-animal standard deviation for number of
 650 stem cells per cross section, $\sigma_{pop} = 1$, intra-animal standard deviation number of stem cells per cross section,
 651 $\sigma = 0.5$, probability of a cell to be proliferative (expected growth fraction), $p_p = 0.5$, inter-animal standard deviation
 652 of p_p , $\sigma_p = 0.04$, probability of a proliferative cell to be mitotic (expected mitotic index), $p_m = 0.015$, inter-animal
 653 standard deviation of p_m , $\sigma_m = 0.003$. (B) Simulations of two adjacent spatially homogeneous zones of
 654 proliferation for 3 animals. Parameters for the anterior zone are the same as in (A). Probability of a cell to be
 655 proliferative and probability of a proliferative cell to be mitotic in the posterior zone are elevated to $p_p = 0.8$ and p_m
 656 $= 0.1$, respectively. The mean switchpoint location is 300 μm anterior to the amputation plane and the
 657 corresponding inter-animal standard deviation is 100 μm . As expected, there are more proliferative and mitotic
 658 cells in the posterior zone. Simulation results can statistically be compared with the cell counts we obtained from
 659 experimentally observed animals to infer growth fraction, mitotic index and switchpoint (Figure 2F-F’’).

660 **Figure 2 – figure supplement 3**



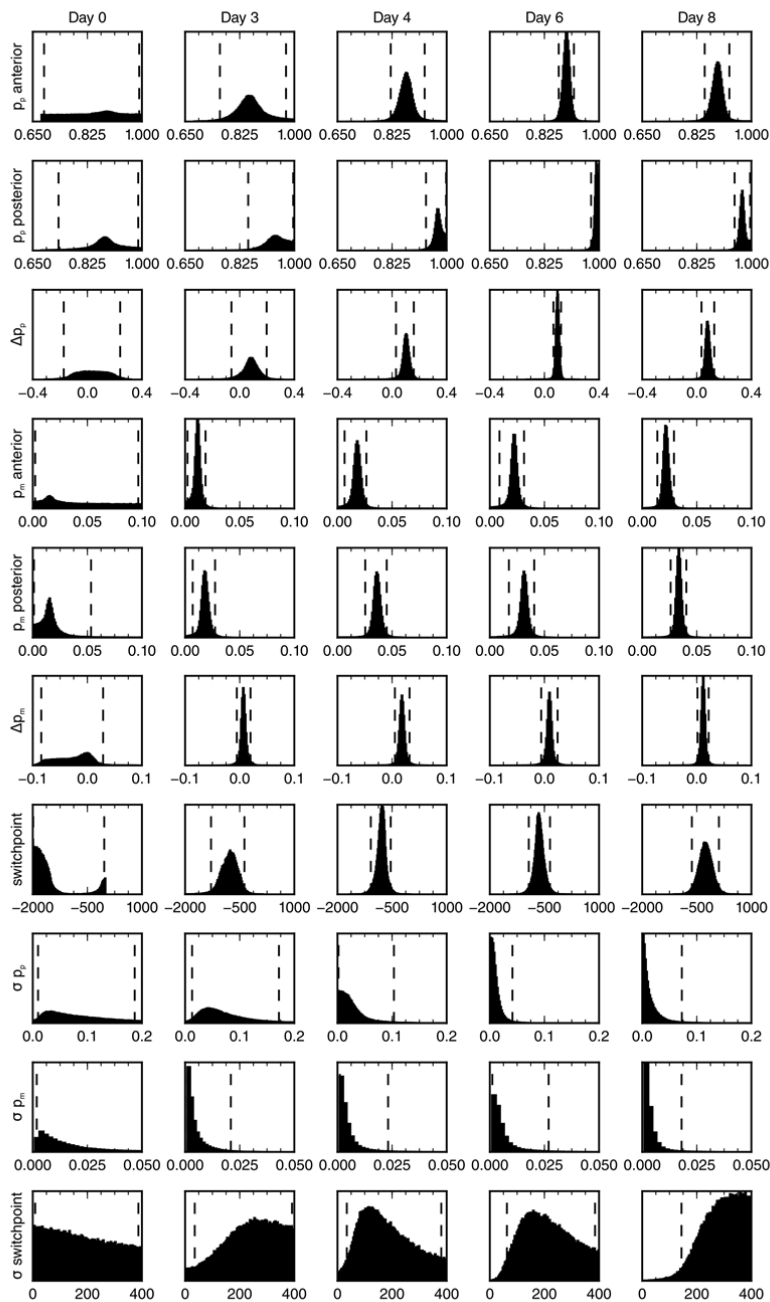
661

662 **Figure 2 – figure supplement 3.** Number of SOX2⁺/PCNA⁺ cells per cross section (upper panel) and mitotic cells

663 per section along the AP axis for all 15 animals. Data from animals 0D_1 and 4D_3 are shown in Figure 2D and

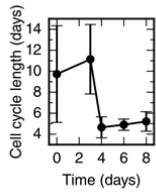
664 2D', respectively. Each row shows data from three animals at a given time point.

665 **Figure 2 – figure supplement 4**



666
 667 **Figure 2 – figure supplement 4.** Posterior marginal distributions for the parameters of the spatial model of cell
 668 counts to analyze the spatiotemporal pattern of proliferation. Each row shows a different model parameter. Each
 669 column shows a different time point. 3 animals per time point were used in the analysis. Vertical dashed lines
 670 show the limits of the 95% credibility interval. The distribution means and the 68% credibility intervals for the
 671 growth fraction, mitotic index and the switchpoint are shown in Figure 2F-F", respectively.

672 **Figure 2 – figure supplement 5**

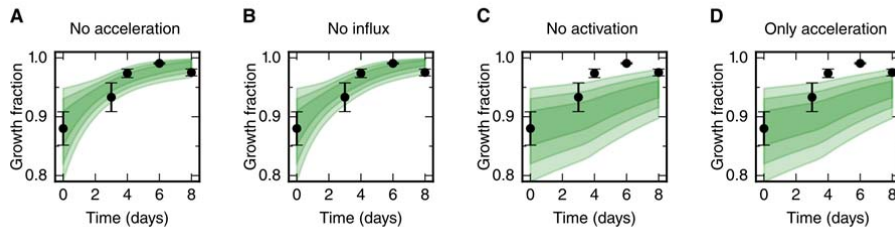


673

674 **Figure 2 – figure supplement 5.** Cell cycle length time-course calculated from the proliferation rate time-course

675 shown in Figure 2G.

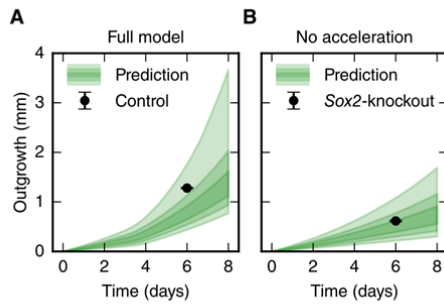
676 **Figure 3 – figure supplement 1**



677

678 **Figure 3 – figure supplement 1.** Prediction of growth fraction in the high-proliferation zone for four model
679 scenarios with selected mechanisms switched off (green shaded areas). Black dots show the same experimental
680 data as in Figure 3B. Scenarios in panels A-D correspond to the scenarios in Figure 3D-G, respectively.
681 Switching off the acceleration of the cell cycle length and switching off the cell influx hardly have an effect on
682 the growth fraction time course (A,B). As expected, switching off the activation of quiescent stem cells has a
683 strong impact on growth fraction time-course (C,D). This is consistent with the fit of a non-zero rate activation rate
684 k to this data.

685 **Figure 3 – figure supplement 2**



686

687 **Figure 3 – figure supplement 2.** Comparison of the spinal cord outgrowth prediction by our model with the
688 measured outgrowth reported by Fei et al., 2014. **(A)** Outgrowth prediction of the full model (green, same as in
689 Figure 3C) and rescaled outgrowth in control condition (black dot, n = 12 axolotls). **(B)** Outgrowth prediction of the
690 model for the case that cell cycle acceleration is switched off (green, same as in Figure 3D) and rescaled, density
691 corrected outgrowth in a Sox2-knockout condition (black dot, n = 24 axolotls).

692 **Additional files**

693 **Supplementary file 1**

694 Tiff stack of individual high-resolution images that are shown in Figure 1 – figure supplement 1

695 (<http://dx.doi.org/10.5281/zenodo.59817>). It can be opened with Fiji or ImageJ.

696 **Supplementary file 2**

697 Zip archives containing all raw images used for the clone tracking

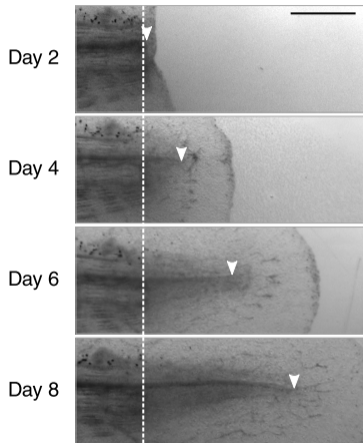
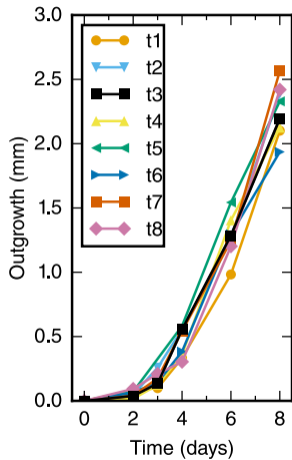
698 (<http://dx.doi.org/10.5281/zenodo.59824>). Images for each individual animal are in separate zip

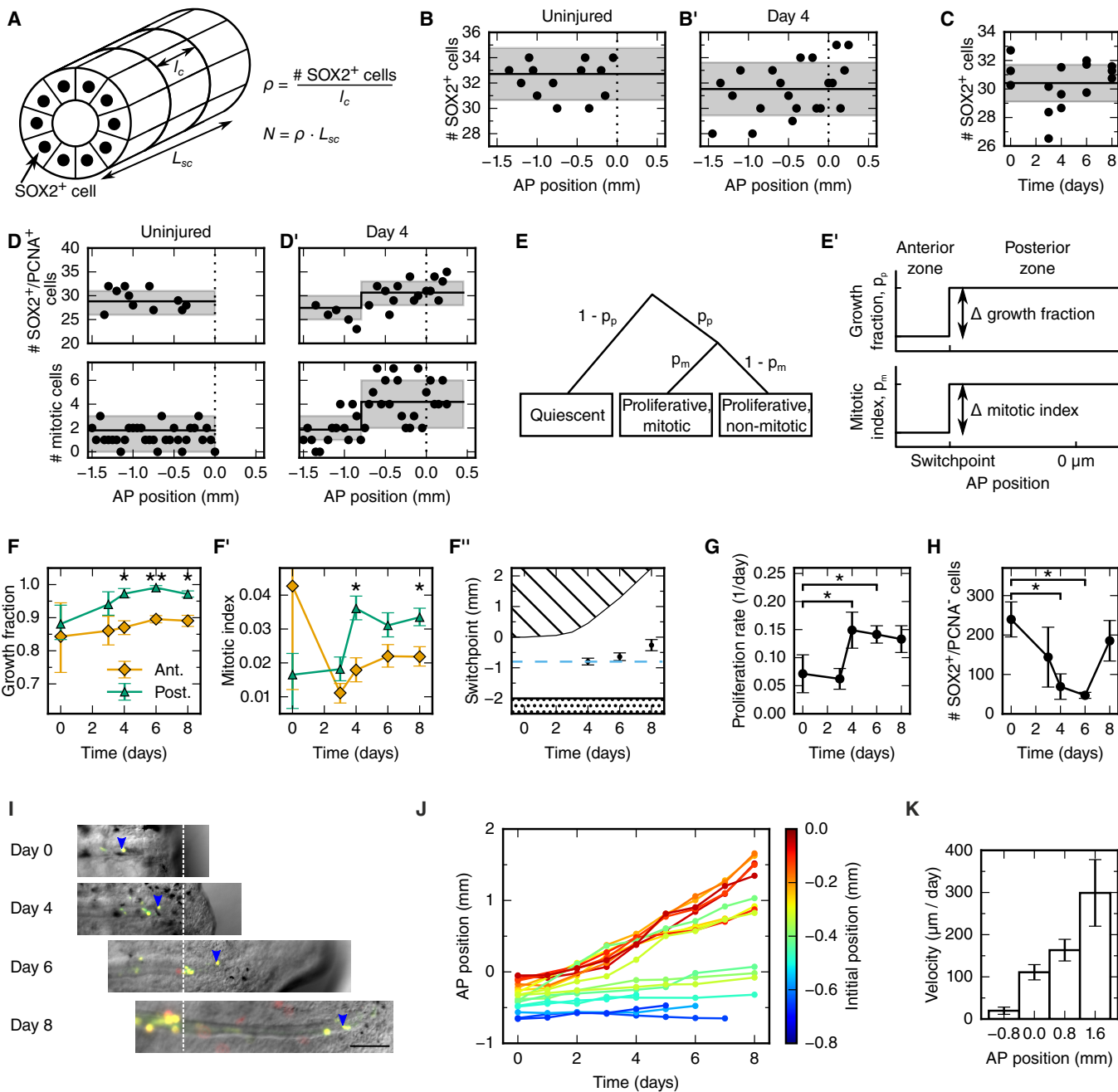
699 archives. Zip archive file names correspond to the arbitrarily chosen animal IDs used in the clone

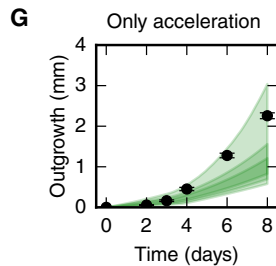
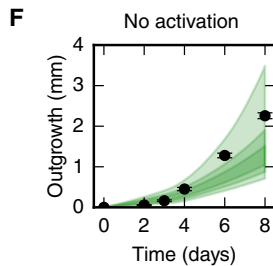
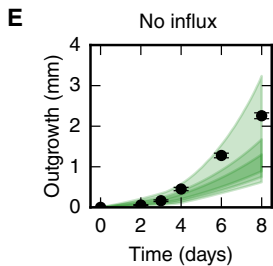
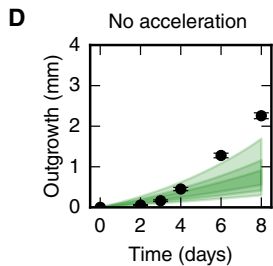
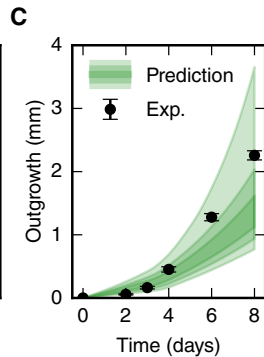
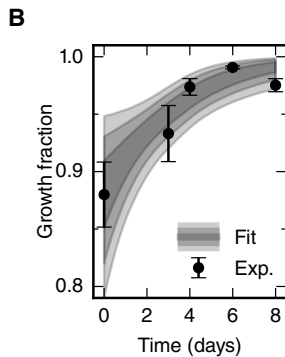
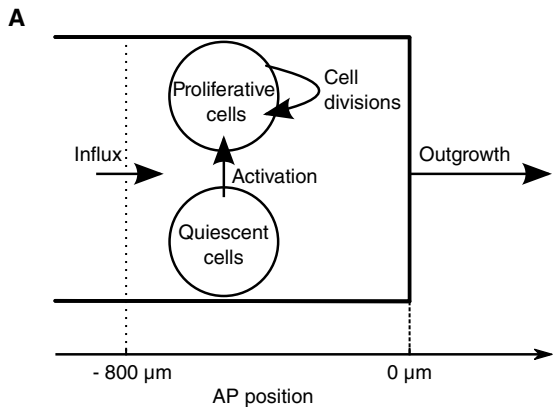
700 trajectory dataset (see Supplementary notebook "clone_velocities"). The image filename indicates the

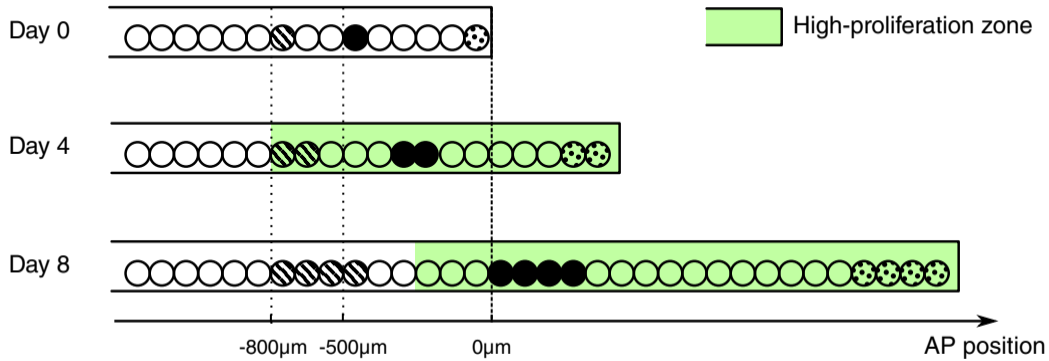
701 time point of the measurement together with the animal ID. A representative example is shown in

702 Figure 2I. The image files can be opened with AxioVision Microscopy software (Zeiss).

A**B**







Day 2

Day 3

Day 4

Day 6

Day 8

Animal t1

Animal t2

Animal t3

Animal t4

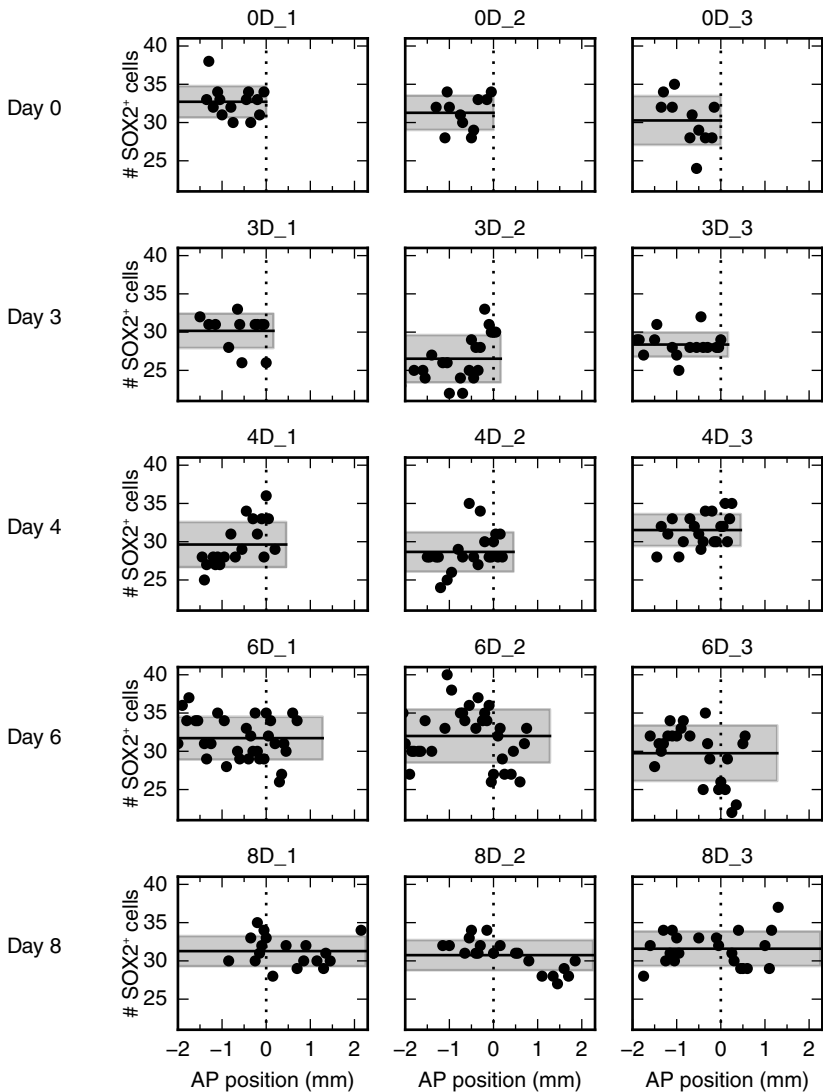
Animal t5

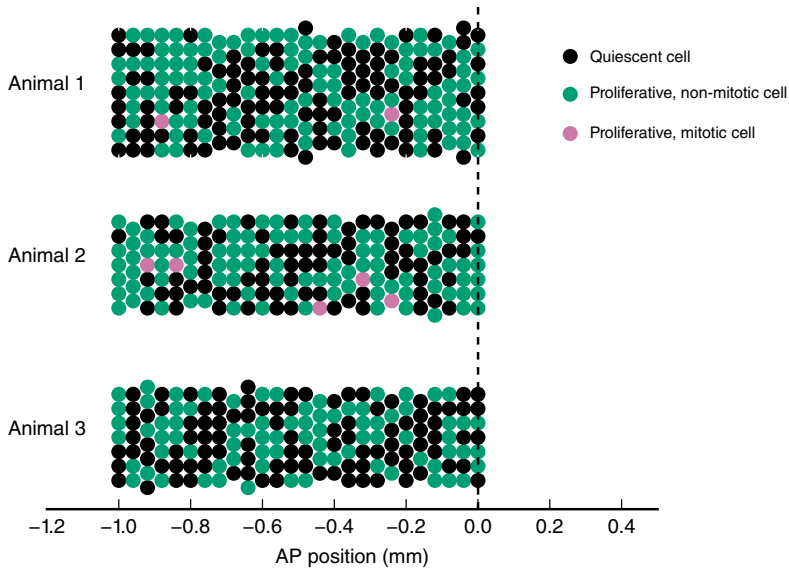
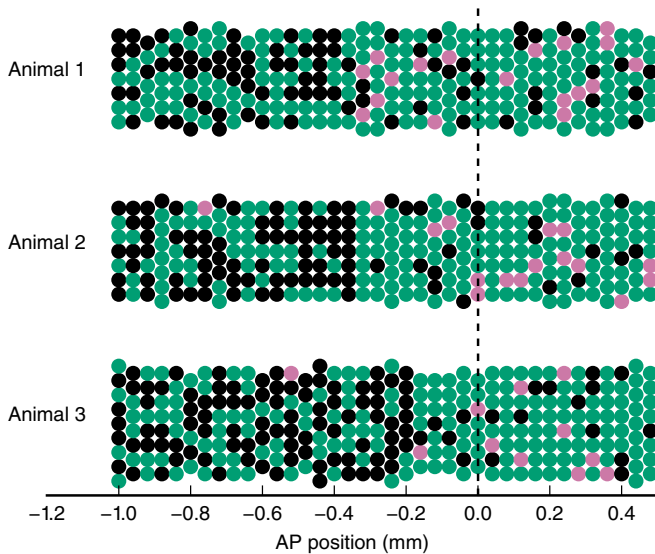
Animal t6

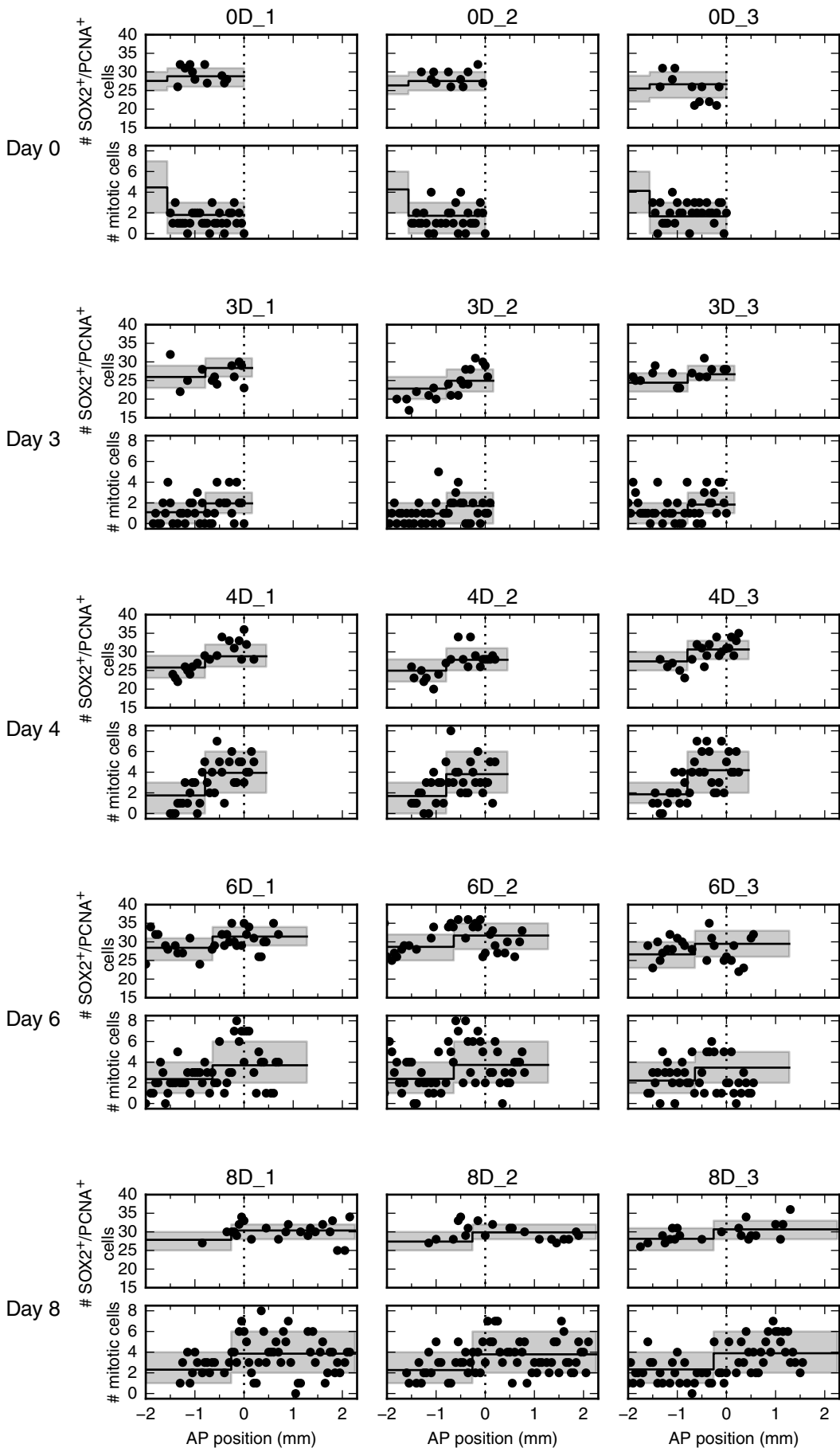
Animal t7

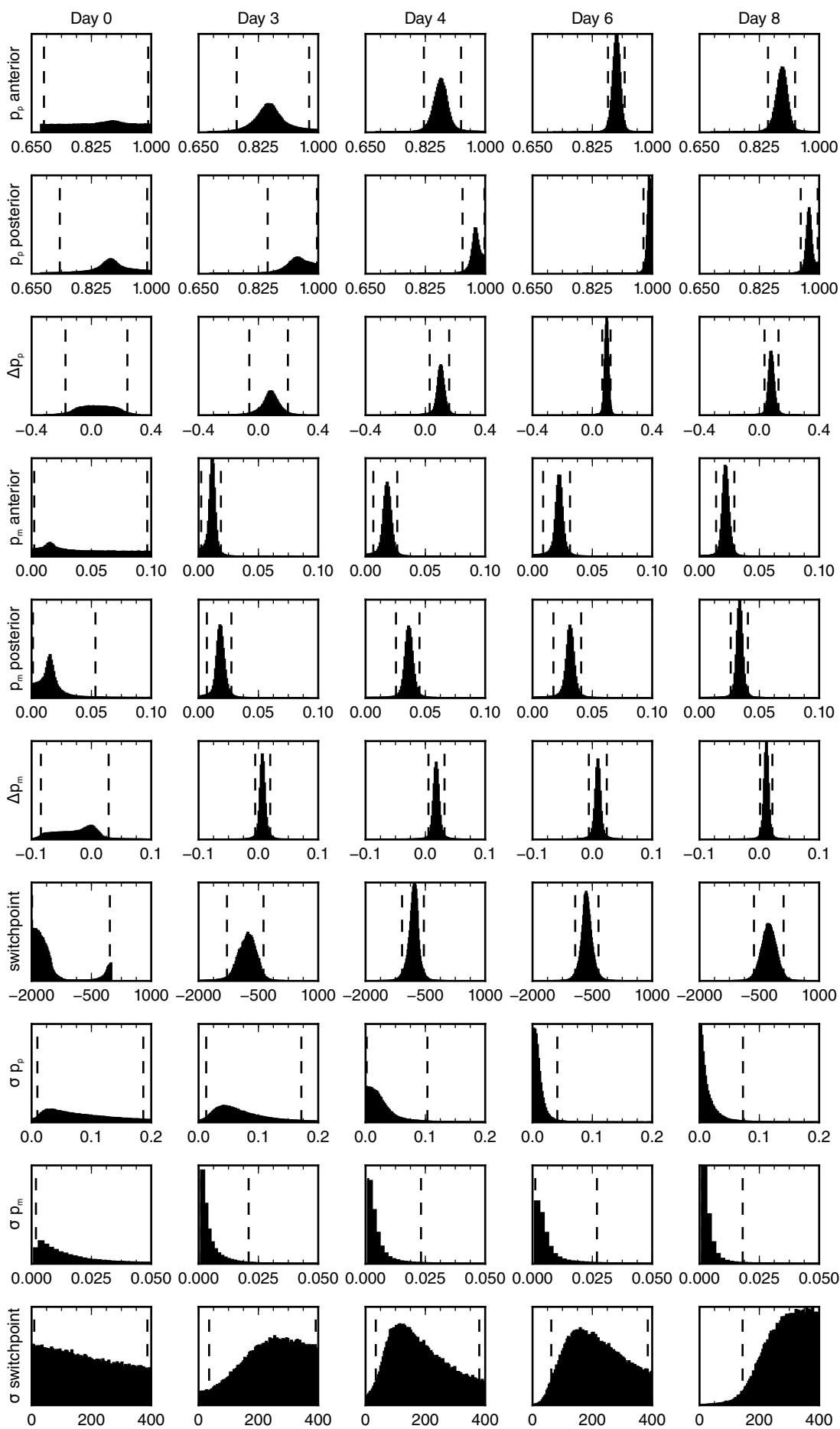
Animal t8

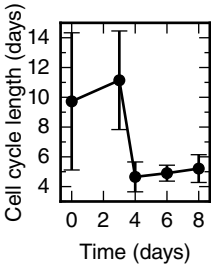




A**B**

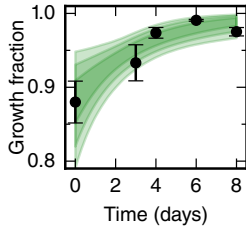




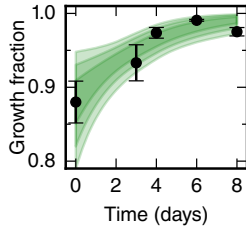


A

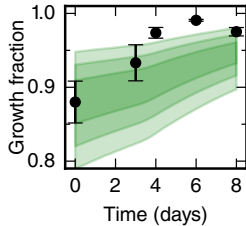
No acceleration

**B**

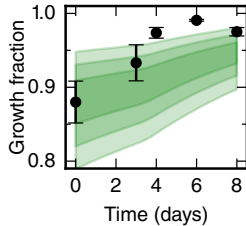
No influx

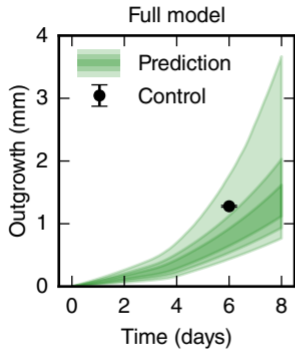
**C**

No activation

**D**

Only acceleration



A**B**